Coordination Chemistry Reviews 443 (2021) 214033

Contents lists available at ScienceDirect

Coordination Chemistry Reviews

journal homepage: www.elsevier.com/locate/ccr

Review

Fabrication and regulation of vacancy-mediated bismuth oxyhalide towards photocatalytic application: Development status and tendency

Jiayin Guo [a,b], Xin Li [a,b], Jie Liang [a,b,*], Xingzhong Yuan [a,b], Longbo Jiang [a,b,*], Hanbo Yu [a,b], Haibo Sun [c], Ziqian Zhu [a,b], Shujing Ye [a,b], Ning Tang [a,b], Jin Zhang [d]

[a] College of Environmental Science and Engineering, Hunan University, Changsha 410082, PR China
[b] Key Laboratory of Environmental Biology and Pollution Control (Hunan University), Ministry of Education, Changsha 410082, PR China
[c] College of Resources and Environment, Hunan Agricultural University, Changsha, 410128, PR China
[d] School of Chemistry and Food Engineering, Changsha University of Science and Technology, Changsha 410114, PR China

ARTICLE INFO

Article history:
Received 25 January 2021
Accepted 9 May 2021

Keywords:
Bismuth oxyhalide
Vacancy
Incorporating approaches
Characterization
Functionality

ABSTRACT

Recently, layered bismuth oxyhalides (BiOX) have been a well-deserved hotspot in the field of photocatalysis owning to their fascinating physicochemical properties derived from unique layered structures. Nevertheless, insufficient sunlight absorption, rapid recombination of electron-hole (e^--h^+) pairs, finite carrier concentration, and weak interaction between BiOX surface and reactant molecules inevitably limit the photocatalytic performance of BiOX. Given this, vacancy engineering, which can unleash the great potential to manipulate crystal and electronic structures and surface chemistry of BiOX, is widely applied to improve BiOX to meet the increasingly diverse theoretical and applicable needs. In this review, we focus on recent development in the design of appropriate vacancies on the BiOX for photocatalytic application. The introduction and analysis of popular vacancies creating approaches for BiOX and techniques to distinguish various vacancies are provided. The inherent functionality of BiOX vacancies in photocatalysis at the molecular level is clarified. Then we present representative photocatalytic applications, performance, and corresponding vacancy behavior of vacancy-mediated BiOX. Finally, based on an unambiguous understanding of the vacancy–property relationships and a complete view of the state of the art of vacancy-mediated BiOX, the future directions and possibilities for the rational design of vacancies to acquire ideal properties are explored.

Contents

* Corresponding authors at: College of Environmental Science and Engineering, Hunan University, Changsha 410082, PR China.
E-mail addresses: liangjie82@163.com (J. Liang), jianglongbo@hnu.edu.cn (L. Jiang).

https://doi.org/10.1016/j.ccr.2021.214033
0010-8545/

1. Introduction

With population and industrialization growth, the increasingly serious environmental pollution and the gradual depletion of fossil fuel reserves have become two major crises in current world [1-4]. Thus, we urgently desire to develop renewable technologies for environmental remediation and energy production. In 1972, Fujishima and Honda discovered the phenomenon of photocatalytic splitting of water on TiO_2 electrodes, which is the preface of photocatalysis [5,6]. Thereafter, tremendous efforts have been devoted to semiconductor-based photocatalysis for various purposes, such as water splitting [7-11], environmental remediation [12-16], CO_2 reduction [17-19], nitrogen fixation [20-23], and organic synthesis [24-26], which are expected to relieve energy and environmental pressures [26-29]. An overall photocatalytic process mainly involves three successive steps [30,31]: light photoexcitation, the subsequent separation and transfer of photoexcited carriers, and the charge carriers consumption via surface redox reactions on semiconductor. In order to better meet the practical application needs, the core issue of photocatalysis is to improve the efficiency of these three steps on the basis of choosing suitable semiconductor-based photocatalyst.

Recently, Sillén-type bismuth oxyhalides BiOX (X = Cl, Br, and I) have received significant attention in photocatalytic field because of their unique hierarchical structure and the indirect optical transition [32-36]. The BiOX series crystallize in the tetragonal matlockite (PbFCl-type) structure (space group P4/*nmm*). The crystal lattice consists of $[Bi_2O_2]^{2+}$ slices sandwiched between double halogen anionic slabs, stacked along the z-axis by the nonbonding (van der Waals) interaction, as shown in Fig. 1a [32]. The (0 0 1) surface of BiOX is of a close-packed structure, while the (0 1 0) surface is of an open channel structure with exposed Bi, Cl, and O atoms (Fig. 1b-c). Besides, the open layered crystalline structure furnishes a sufficient space to polarize the related atoms and orbitals and induces an internal static electric field perpendicular to the $[Bi_2O_2]^{2+}$ slices and $[X]^-$ slabs, which favors the separation of photogenerated electrons and holes [33,37,38]. The indirect-transition bandgap implies that the photoexcited electrons have to pass through a certain k-space distance during the emission, so the recombination probability of photoinduced carriers is reduced [39]. Moreover, the band gap of BiOX diminishes with the increase of atomic number of X atoms (Fig. 1d). Accordingly, the light absorption range can be extended from the ultraviolet region to the visible region. Specifically, BiOCl with a large band gap (~3.2 eV) only responses to ultraviolet light, resulting in its deficient photo absorption [40]. BiOBr (~2.7 eV) and BiOI (~1.7 eV) both exhibit visible-light-driven photocatalytic performance. However, their photocatalytic performance remains suboptimal owning to the rapid recombination of photoexcited carriers and reduced redox capacity. Therefore, it is hard for BiOX to simultaneously maintain sensitive light responsiveness, excellent carrier migration, and strong redox ability. In addition, the photocatalytic efficiency of BiOX is limited by the unresponsive carrier-induced surface reactions [41]. For example, the limited surface reactive sites for CO_2 binding is inevitably hinders the CO_2 reduction efficiency of BiOCl [42].

The vacancy is a typical point defect originating from the disappearance of atoms in lattice positions. The valence band (VB) of BiOX is mainly occupied by O 2p and X δp (X = Cl, Br, and I, and the corresponding δ are 3, 4, and 5, respectively) states, whereas the conduction band (CB) is occupied by Bi 6p states (their transition is from O 2p and X δp to Bi 6p orbitals) (Fig. 1d) [43]. This unique electronic structure makes that no matter what kind of atom (Bi, O, or X = Cl, Br, and I) is missing, the formed vacancy in its corresponding lattice position will influence the physicochemical properties of BiOX significantly. Therefore, vacancy engineering stands out in terms of tuning the electrical structure of BiOX, thereby exerting influence on the intrinsic properties of BiOX. Furthermore, the vacancies formed on the surface of semiconductor can change the electronegativity of the BiOX or generate localized electrons, thus promoting the redox reaction on the semiconductor surface [44,45]. In brief, a rational introduction of well-defined and appropriate vacancies is beneficial for ameliorating the three limiting steps in the process of BiOX photocatalysis. Consequently, vacancy-mediated BiOX with enhanced performance is widely applied in the photocatalytic field. However, vacancies do not always bring good impacts, as the conditions of vacancies' location and quantity regulate the effects together [46,47]. Moreover, vacancies also suffer from the disadvantage of instability. For example, during the reduction of carbon dioxide, oxygen vacancies will be filled with oxygen atoms generating from dissociation of CO_2 [42].

To date, several reviews on BiOX and/or vacancies have been published. Ye et al. gave an overview of the synthesis, modification strategies and photocatalytic degradation application of BiOX [48,49]. Li et al. focused on the layered structure dependent properties of BiOX [32]. Li et al. elucidated the inherent functionality of OVs in water splitting, hydrogen peroxide decomposition, reactive oxygen species formation, and ammonia synthesis using 2D BiOCl as the platform [50]. Liu et al. reviewed that vacancies possess the potential to manipulate the electron and phonon structures of two-dimensional inorganic Materials [51]. Li et al. emphasized vacancy engineering for modulating electronic structures and metal–insulator transitions, and introducing magnetism in non-magnetic materials [52]. As seen from the published reviews, the BiOX-based materials have received more and more attention, and vacancy engineering has been a promising approach for modifying the performance of catalysts. However, the application of vacancy engineering for manipulating the photocatalytic performance of BiOX has not been systematically reviewed up to now. Due to the unique electronic structure of BiOX and its popularity in the field of photocatalysis, it is crucial to summarize and analyze the current status of BiOX containing vacancies based on the existing researches, which can pave the way for rational use of vacancy defects in BiOX to regulate their photocatalytic behavior.

In this review, we highlight the power of vacancy engineering to tailor the properties of BiOX. We firstly summarize the existing methods and mechanisms of introducing vacancies into BiOX so as to let these methods be better applied or improved. Simultaneously, in order to better understand the vacancies, advanced characterization methods including computational characterization are presented. Furthermore, the roles of vacancy engineering in improving each step of a photocatalytic process from the perspective of fundamental mechanisms are expounded, followed by the introduction of recent progress of vacancy-mediated BiOX in photocatalytic applications. Finally, the existing challenges and future development trends of BiOX vacancy engineering are put forward. We hope that this review based on the vacancy engineering of BiOX can not only facilitate the development of BiOX photocatalytic performance, but also inspire the vacancy design of other photocatalysts, thus greatly boosting the development of photocatalysis.

2. Incorporating approaches of vacancies in BiOX

Thus far, many feasible and controllable strategies have been developed to design vacancy in BiOX. According to the formation sequence of vacancy relative to BiOX material body, we classify the fabrication of vacancy into two kinds of approaches: "top-down" and "bottom-up" (Fig. 2). Top-down approaches synthesize vacancy-mediated BiOX from a pre-formed virgin BiOX material by post treatment. Bottom-up approaches fabricate vacancy-mediated BiOX by one-step method from molecular precursors, where vacancy is built-in with the crystal growth.

2.1. Top-down approaches

Light irradiation method. Light irradiation is generally applied to introduce oxygen vacancies (OVs) on BiOX, which is a facile method to introduce OVs due to the low bond energy of surface

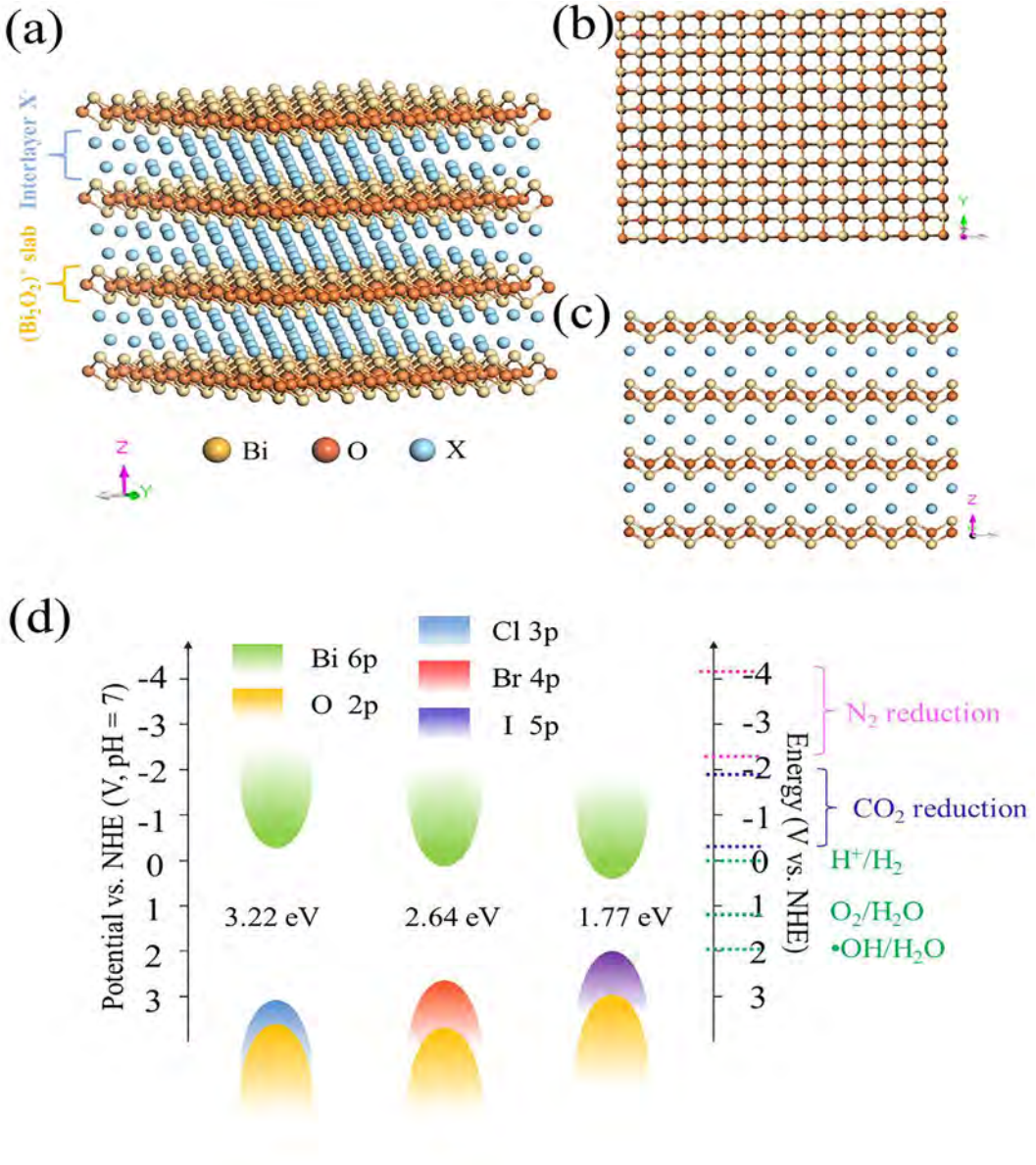

Fig. 1. Crystal structure of BiOX (X = Cl, Br, I) (a) three-dimensional projection; (b) (0 0 1) surface; (c) (0 1 0) surface. (d) Schematic valence and conduction band structures of BiOX (X = Cl, Br, I), where the data were taken from previous reports, [43,183,184]. The orange, blue, red, and purple boxes, respectively, represent the bands from O 2p, Cl 3p, Br 4p and I 5p orbitals, and the green box shows a conduction band composed mainly of Bi 6p, according to DFT calculations.

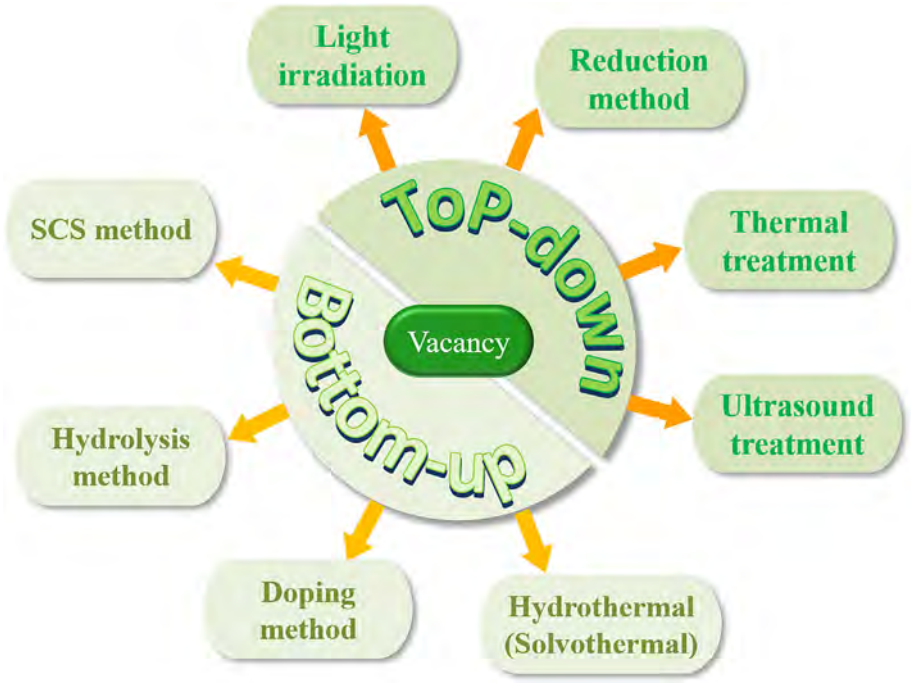

Fig. 2. Schematic illustration of vacancies introduction approaches.

Bi-O bond and their low formation energy [53,54], and the amount of vacancies can be regulated by irradiation time [55]. In 2011, Ye et al. [56] first used high-energy UV light irradiation to produce OVs on BiOCl. They attributed the formation of OVs to the long Bi-O bond with low bond energy. Thereafter, they found that, during the irradiation process, the inert gas blowing and short-wavelength light illumination are conducive to the generation of OVs [55]. Based on the interpretation of Ye et al., Li et al. [57] further put forward that the generation of OVs on BiOCl by light illumination mainly involves three steps. Firstly, the layered structure of BiOCl inhibits the recombination of carriers, and thus facilitating the trapping of UV light-induced holes (h^+) by the surface lattice O along the [001] direction, then O anions are partially neutralized through the $O^{2-} + h^+ \rightarrow O^-$ reaction. Secondly, (001) facets of BiOCl providing O-rich environment together with long and weak Bi-O bonds favor the OVs formation by capturing h^+ with two adjacent O anions ($(O–O)^{4-}$) on the bridging rows via the reaction of $(O–O)^{4-} + 4\ h^+ \rightarrow O_2$, releasing O_2 and leaving behind OVs on the surface. Finally, BiOCl can generate OVs at ambient conditions with UV light. However, Wu et al. [58] pointed out that the above explanation is not comprehensive since it cannot well explain why the content of OVs on BiOCl could reach saturation under continuous UV illumination. They concluded that the surface hydroxyl groups play a critical part in the generation process of photoinduced OVs on BiOCl. As shown in Fig. 3a, the Bi-O bond length on the perfect O-terminated (001) surface is 2.196 Å, while the Bi-O bond length on the hydroxylated surface is 2.293 or 2.315 Å. Besides, Fig. 3a (the bottom two) also exhibits that the existence of hydroxyl groups on BiOCl greatly suppresses the electrons overlapping of Bi and O, which indicates that the energy of the adjacent Bi − O bond is reduced with the existence of hydroxyl groups. Thus, the existence of surface hydroxyl groups facilitates the formation of OVs under UV light illumination (Fig. 3b). Furthermore, it should be noted that OVs on BiOX are easily to be repaired. For example, O atom produced by CO_2 dissociation during CO_2 photoreduction is considered to repair the OVs (Fig. 3c) [42]. Because of the instability of OVs, the regeneration of OVs on photocatalysts calls for special attention.

Reduction method. The most popular reduction methods involved in the introduction of OVs into BiOX are chemical reduction strategy and electroreduction strategy. Chemical reduction strategy creates OVs by treating pre-formed BiOX with reductants. The H from the reductants can interact with lattice oxygen to form OVs. H_2 [59–61], $NaBH_4$ [62,63], and KBH_4 [64] are frequently used reductants. In the process of chemical reduction, the content of vacancies can be controlled by controlling the concentration of reductants [62]. The electroreduction strategy is processed by applying a voltage in a three-electrode cell with as-prepared BiOX as the working electrode [54,65]. For instance, Bai et al. synthesized BiOI rich in OVs by applying a voltage of 0.6 V vs Ag/AgCl for 25 min in a three-electrode cell with a $BiVO_4$ counter electrode [65]. Fig. 3d exhibits the detailed formation process of BiOI with OVs.

Note that most reduction methods, due to their lack of selectivity, will result in the production of metallic bismuth on BiOX. For instance, when three-dimensional hierarchal BiOI is treated with $NaBH_4$ as a chemical reducing agent, OVs and Bi nanoparticles are simultaneously introduced into BiOI [62]. Although the introduction of appropriate metallic bismuth is beneficial to the improvement of photocatalytic activity, it is adverse to understand the specific role of OVs. Furthermore, it has been reported that the extraction of Bi ions from the cationic sites will lead to the formation of BiVs on Bi_2MoO_6 during the reduction process [66]. However, the similar phenomenon has not been involved in the study of vacancy-mediated BiOX prepared by reduction method, which requires further research.

Thermal treatment. Thermal treatment is a common method to introduce OVs and iodine vacancies (IVs). High temperature facilitates the bond cleavage and accelerates the escape of atoms from lattice. It is generally believed that the thermal treatment for the purpose of producing OVs is best carried out in an oxygen-deficient environment because the generated OVs will be re-oxidized in the oxygen-rich atmosphere [45,67]. For instance, Wang et al. introduced OVs into BiOBr via annealing in vacuum conditions (~10^{-3} Pa) at 300 ℃ for 3 h [67]. However, some studies have introduced OVs by directly calcinating in air atmosphere [68–

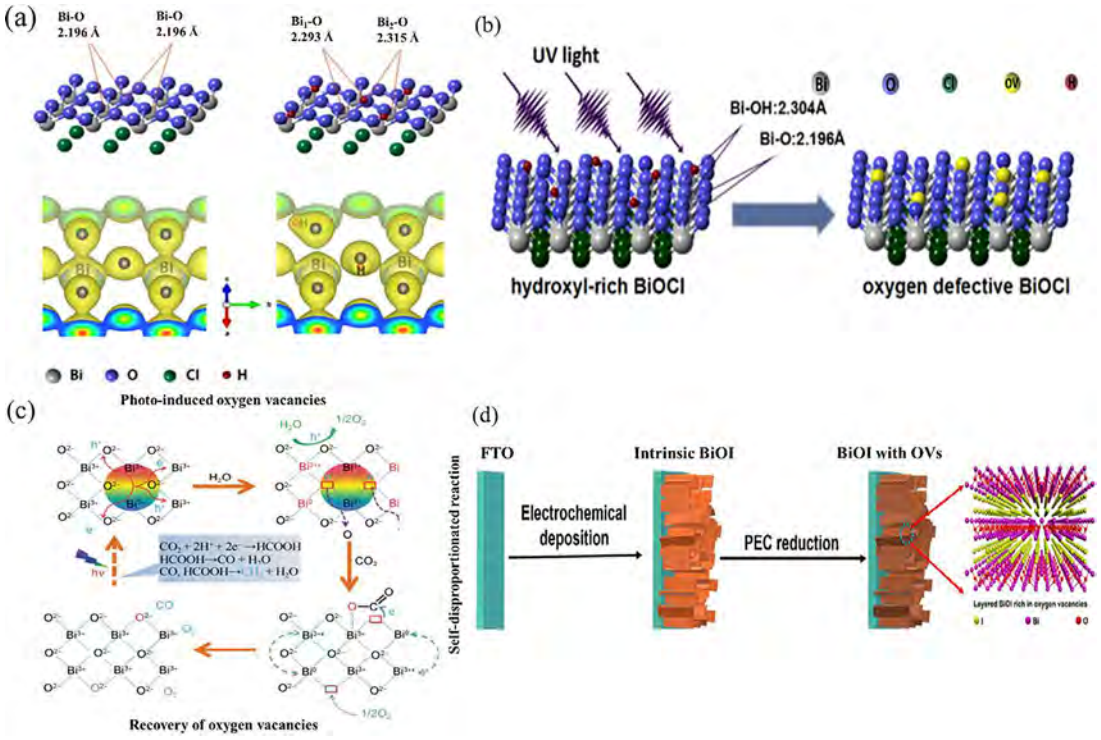

Fig. 3. (a) Schematic view of the Bi-O bond length and representation of charge density distribution along the O-terminated (001) surface of BiOCl: clean surface (left) and hydroxyl-rich surface (right). (b) The proposed OVs formation mechanism of BiOCl with surface hydroxyl groups under UV light irradiation. Reproduced with permission [58]. Copyright 2017, American Chemical Society. (c) Possible mechanism of OVs repair and recovery. Reproduced with permission [42]. Copyright 2014, Tsinghua University Press and Springer. (d) Electroreduction strategy process for introducing OVs on BiOI. Reproduced with permission [65]. Copyright 2019, Elsevier.

70]. For example, Cui et al. found that OVs could be generated by annealing BiOCl in the air atmosphere, and the best photocatalytic efficiency was obtained when the annealing temperature was 450℃ [69]. In the process of heat treatment, the effect of gas atmosphere on vacancy formation needs further discussion.

In addition to OVs, high temperature of thermal treatment also impel a portion of iodine elements to volatilize from the BiOI crystals because of the weak interlayer van der Waals forces and the volatility of iodine, resulting in the formation of IVs [37,71,72]. For example, Wang et al. smoothly introduced IVs by heating hydrothermally prepared BiOI samples in air. Besides, the amount of IVs in the BiOI nanosheets was adjusted by controlling the heating temperature [73]. Similarly, Yang et al. successfully prepared I-deficient BiOI nanosheets by calcination in air with temperature of 340 ℃ [71].

Ultrasound treatment. Cavitation effect in ultrasonic process can produce local pressures as high as 500 atm and local temperatures as high as 5000 K, with a heating and cooling rate larger than 10^9 K/s [74]. Besides, shock waves and high-speed inter-particle collisions generated in ultrasonic process can directly impact photocatalysts, leading to the formation of surface OVs [75]. Therefore, ultrasound treatment has been applied to introduce OVs into BiOX. Fan et al. successfully introduced OVs onto as-prepared BiOI nanosheets at room temperature by a low-frequency ultrasound device [76]. The concentration of OVs can be regulated by the ultrasonic time, which further influences the photocatalytic activity. In the research of Fan's group, the BiOI nanosheets underwent 15 h ultrasound treatment possess the best photocatalytic activity, and too long or insufficient ultrasound time both cannot achieve the ideal photocatalytic effect [76]. However, 15 h of ultrasonication treatment is generally considered to be time-consuming and energy-consuming. Recently, Wu et al. adopted a probe sonic tip to treat hydrothermally prepared BiOCl in a water-cooled bath at 25℃ for 30 min [77]. The rigid transient heat and pressure effect of probe sonic tip can effectively dislocate the O atoms from the lattice of BiOCl in a short time.

2.2. Bottom-up approaches

Hydrothermal (Solvothermal) reduction treatment. During the process of hydrothermal (solvothermal) synthesis of BiOX, a reducing environment is critical to the formation of OVs. Oxygen-terminated BiOX surfaces can easily react with reductive glycol to produce OVs, because alcohol groups of glycol can react with the oxygen to produce acid and aldehydes which can further react with glycol to yield organic by-products [78]. Jiang et al. detected these organic by-products through GC–MS analysis, which confirmed that ethylene glycol did react with the surface oxygen atoms [78]. Shiraish et al. prepared BiOCl OVs and perfect BiOCl in autoclaves at 160℃ for 12 h with glycol and water as solvent, respectively, which further proved the important role of ethylene glycol in OVs formation [79]. Ethanol and glycerin with similar properties to glycol, are also commonly used as solvents for OVs generation [80–82].

It should be noted that the reducing atmosphere at high temperature inevitably introduces massive OVs at the interior of the BiOX which can serves as recombination center of e^--h^+ pairs, and the high viscosity of polyols generally limits the specific surface areas of BiOX. Thus, a mixed solvent strategy has emerged, where the addition of water makes the BiOBr nanocrystals nucleate faster than the reduction reaction induced by the reductive solvent, resulting the completed growth of nanosheets before the formation of OVs [47]. Therefore, the OVs are mainly constructed on the surface of BiOX instead of within the bulk.

During the hydrothermal (solvothermal) processes, the assistance of microwave is effective for the generation of OVs, since

its intense localized heating effects can break the Bi-O bonds, leading to the formation of OVs on BiOX [83]. Sun et al. synthesized BiOCl through microwave-assisted solvothermal, hydrothermal, and precipitating methods, respectively [83]. XPS results show that the BiOCl synthesized by microwave assisted synthesis has the largest area ratio of adsorbed oxygen species to crystal lattice oxygen, which can roughly estimate that microwave solvothermal method can induce more surface OVs on BiOCl. There are two main reasons for this phenomenon. One of the reasons is that microwave irradiation promotes the formation of BiOCl nanosheets with exposed (001) facets, which is favorable for the formation of OVs as its high oxygen atom density [56]. Another reason is that the intense local heating effect leads to the ultrafast crystallization with surface defects.

In addition to OVs, BiVs and IVs can also be introduced by solvothermal treatment. For example, in the solvothermal synthesis of BiOI, glycerin can lead to the formation of IVs, which may be due to the fact that hydroxyl groups in glycerol can combine with I ions at high temperature, taking I ions away from BiOI lattice and leaving IVs [84]. Teng et al. [85,86] introduced BiVs into BiOCl in a solvothermal environment at 180℃ by using Bi_2O_3 and NH_4Cl as precursors and H_2O_2 as solvent. Meanwhile, pristine BiOX was prepared with $Bi(NO_3)_3{\cdot}5H_2O$ and NaCl as precursors and glycol as solvent in a solvothermal environment at 170℃. It can be inferred that the formation of BiVs is closely related to the precursor substances and solvothermal conditions, however, the reasons for the formation of BiVs remains to be further explored.

Morphology control. Considering the crystal structure of BiOX (Fig. 1a), the construction of ultrathin 2D nanosheets (2D engineering) is conducive to the formation of Bi vacancies (BiVs) because the external Bi atoms are easier to escape from the lattice than the inner O atoms [44,87]. For example, Di et al. synthesized ultrathin BiOBr nanosheets with thickness of around 1.2 nm at room temperature by the control of the long carbon chain $[C_{16}mim]Br$ [87]. The STEM images show that partial surface Bi atoms of the ultrathin BiOBr nanosheets are missing, while the thicker counterpart exhibits an ordered surface atomic arrangement, which confirms the crucial role of reducing the thickness of nanosheets for the formation of BiVs. However, Xie group reported that BiOCl nanosheets with the thickness of 30 nm possess isolated BiVs, and when the thickness of the nanosheets is further reduced to atomic scale (2.7 nm) the BiVs are changed to triple vacancy associates ($V'''_{Bi}V^{\bullet\bullet}_{O}V'''_{Bi}$) [44]. This phenomenon can be ascribed to that the external Bi atoms are easier to escape from the lattice than the inner O atoms, but as the thickness of the nanosheets decreases, the escape of the buried internal oxygen atoms becomes easier [44]. Therefore, they consider that the types of surface vacancies can be tuned by adjusting the thickness of semiconductor nanosheets. We think that the difference between these two researches is mainly due to the different synthesis conditions. The experiment of Di et al. was carried out at room temperature, which is difficult to generate vacancies, while the experiment of Xie et al. was carried out under solvothermal conditions with a temperature of 160 °C. Therefore, even the thicker nanosheets (30 nm) prepared by Xie et al. possess BiVs, and further reducing the thickness of the nanosheets will produce large vacancy associates.

More importantly, in the process of introducing the OVs by hydrothermal (solvothermal) method, controlling the formation of ultrathin 2D BiOX nanosheets is icing on the cake, and even the content of vacancies can be dominated. Zhang et al. calculated that that the formation energy of OV (E_{fOV}) for ~3.4 nm BiOCl nanosheets is 2.09 eV, while that of ~8.8 nm BiOCl nanosheet is 2.37 eV through series of DFT calculations [46]. The formation energy of OVs confirmed that ultrathin BiOCl nanosheets are easier to introduce surface OVs than its thicker counterpart. In general, the thickness of the BiOX nanosheets can be well controlled by adding surfactants. A typical case is that Sun et al. synthesized BiOCl with different OVs content by using ammonium sulfamate as surfactant [88]. The detailed regulatory mechanism can be explained by Fig. 4a. During the hydrothermal process, BiOCl tends to form layered structure with their inherent crystal properties. At the same time, ammonium sulfamate can easily be adsorbed on BiOCl (001) facets for its appropriate surface energy and inhibits the growth along [001] direction. However, by increasing the pH, the ammonium sulfamate molecules decompose, thus weakening the inhibition effect. Therefore, with the assistance of ammonium sulfamate, the thickness of BiOCl can be modulated by controlling the pH value, so as to realize the regulation of the OVs content. Besides, as a typical polymetric surfactant, polyvinylpyrrolidone (PVP) is commonly used to control the formation of ultrathin BiOX nanosheets. PVP serves as a capping agent which can selectively deposit on {001} planes at the top and bottom, thereby preventing the axial growth of BiOX [29]. For example, Xue et al. synthetized BiOBr nanosheets (Fig. 4b) with desirable OVs via the addition of PVP in the synthesis process, while OVs absent in the BiOBr nanoplates (Fig. 4c) which were synthesized by the same process but without adding PVP [89].

Furthermore, curving 2D nanosheets to form a tubular structure inevitably leads to surface structure distortion, thereby resulting in the escape of partial surface oxygen atoms and leaving behind OVs [90,91]. Therefore, the construction of BiOX nanotubes is a potential way to build surface OVs. However, there has been few researches on the tubular structure of stoichiometric forms BiOX. Hydrothermal (solvothermal) preparation of BiOX nanotubes often combines with Bi-rich strategy, pH regulation and surfactant assistance [91,92]. For example, Lin et al. reported that by regulating the PVP concentration and pH value of the hydrothermal reaction system, the final products can be tuned from BiOI nanosheets to Bi_5O_7I nanotubes and Bi_5O_7I nanobelts, thereby they successfully prepared Bi_5O_7I nanotubes with rich OVs. [91]. Besides, Di et al. prepared $Bi_{12}O_{17}Br_2$ nanotubes by a one-pot facile solvothermal method with the assistance of PVP at the pH value of 12.5 [93]. The resulting $Bi_{12}O_{17}Br_2$ nanotubes contain higher OVs concentration than the plate-like $Bi_{12}O_{17}Br_2$. This is attributable to the weakened Bi − O bond of the stretched atomic structure on the curved surface, thus the escape of oxygen atoms and the creation of OVs become easier.

Doping method. Ions doping process will distort the crystal structure and destroy the charge balance, thereby inevitably creating vacancies. Zhong et al. and Liu et al. discovered that doping Fe atoms into BiOX nanosheets induced the formation of OVs in their vicinity [94,95]. Because of the overall charge balance in the crystal, cationic Fe substitutes for Bi. The size difference between Bi and Fe atoms causes structural distortion, and the subsequent crystal relaxation leads to the formation of OVs. The theoretical calculation reveals that the formation energy of OVs is smaller when it is connected with Fe (2.45 eV) than only with Bi (3.30 eV). Therefore, OVs tend to form around Fe in Fe doped BiOBr. Additionally, Zhang et al. revealed that in the process of optimizing the dipole moments by substituting the bromine atoms with iodine atoms in BiOBr, a few dangling bonds were generated in the covalently bonded layers, which leadead to the generation of OVs on $[Bi_2O_2]^{2+}$ layers [96]. It is reported that IVs can also be introduced by doping method. Specifically, Zeng et al. reported that the doped carbon in BiOI can lead to the loss of partial terminal I atoms in the [I-Bi-O-Bi-I] unit and generate corresponding vacancies [97].

Hydrolysis method. Hydrolysis method prepares vacancy controllable BiOX by regulating the precipitant process, which is easy to operate. Song et al. realized the OVs control by regulating pH via the addition of different alkali sources [98]. However, the mecha-

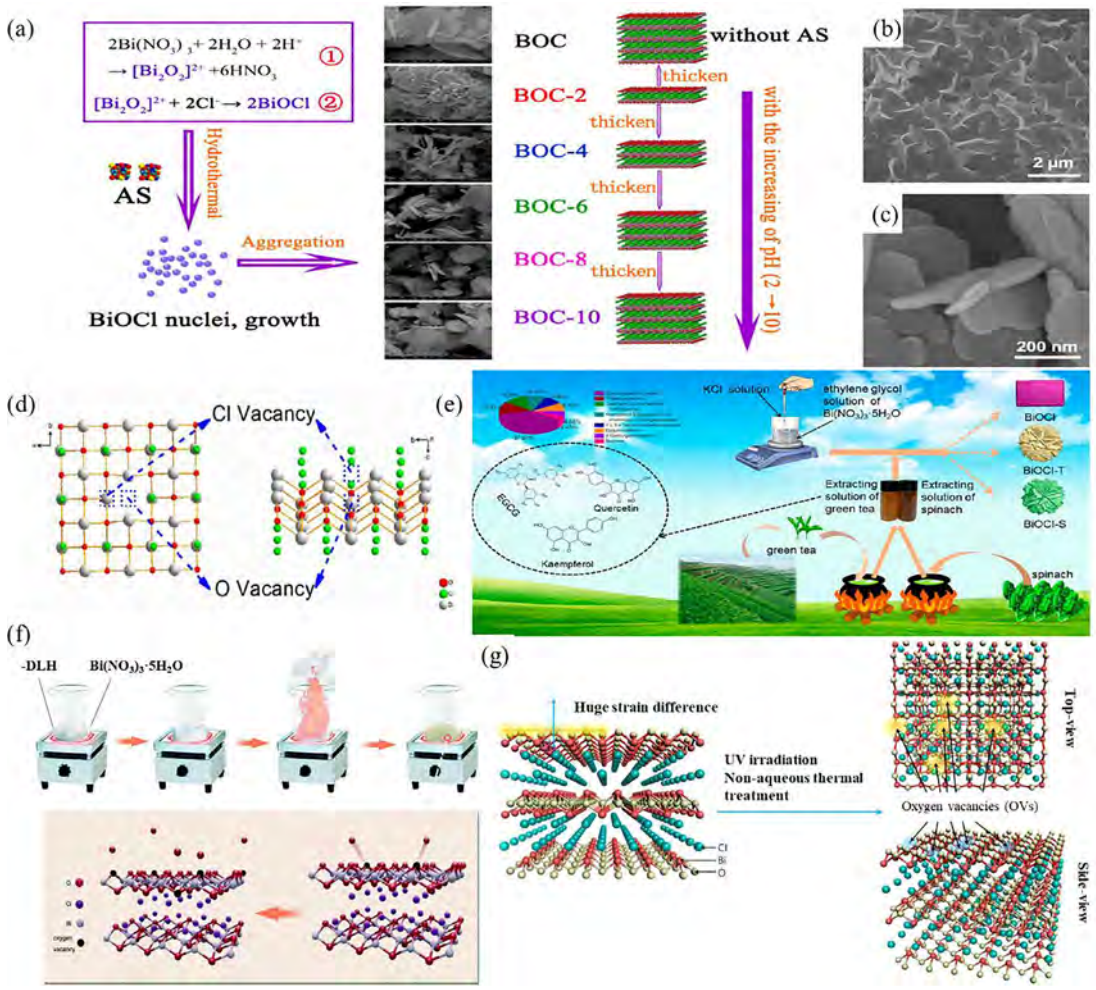

Fig. 4. (a) The possible formation mechanism of BiOCl samples. Reproduced with permission [88]. Copyright 2018, Springer. (b-c) SEM images of the OVs-BiOBr nanosheets and BiOBr nanoplates, respectively. Reproduced with permission [89]. Copyright 2018, American Chemical Society. (d) Crystal structures of BiOCl with O and Cl dual-vacancies. (e) Synthetic scheme for BiOCl with O and Cl dual-vacancies. Reproduced with permission [99]. Copyright 2018, American Chemical Society. (f) Schematic formation route of surface OVs in BiOCl during the SCS process. Reproduced with permission [101]. Copyright 2016, Royal Society of Chemistry. (g) Surface OVs formation on layered BiOCl. Reproduced with permission [43]. Copyright 2016, American Chemical Society.

nism of OVs formation regulated by pH changes in the hydrolysis process needs to be further explored. Besides, the addition of reducing substance in the hydrolysis process can also induce the formation of vacancies. Interestingly, Li et al. [99] innovatively adopted extracting solutions of spinach and green tea as reductants to produce chlorine and oxygen dual vacancies on BiOCl (Fig. 4d). This green scheme (Fig. 4e) is easy to operate, which mainly takes advantage of high content of polyphenol with strong antioxidant capacity contained in green leaves.

Solution combustion synthesis (SCS) method. The SCS process can balance the oxygen in the crystal lattice and that in the external atmosphere by emitting the oxygen atoms in the lattice when the external oxygen pressure is low enough, thus leaving OVs in the lattice [100,101]. Li et al. employed ionic liquids (ILs) as combustible solution to fabricate OVs in BiOX [100,101]. In the process of ILs combustion, oxygen deficiency and high temperature circumstance are formed, which is conducive to oxygen atoms escaping from the lattice surface to form OVs. The solution combustion synthesis starts by mixing precursors and heating them on an electric furnace until the formation of a uniform white solution (ILs). ILs are formed via the coordination of ammonium chloride salts and metal nitrates. Then, the ILs are heated in an oxygen atmosphere tubular furnace to obtain the target product. The potential formation route of OVs by SCS method is exhibited in Fig. 4f.

Altogether, each incorporating method has its own merits and demerits. Table 1 summarizes and compares these approaches for incorporating vacancies into BiOX. Besides, it should be noted that most top-down approaches only facilitate the removal of atoms from the surface of photocatalysts. For example, under the action of external heat and light energy, the differences in strain between strong in-plane bonding and weak out-of-plane interactions make the external atoms more easily escape from the mother crystal than the inner atoms (Fig. 4g) [42,43]. Chemical reduction process also prefers to distribute vacancies on the surface, because the penetration depth of reductants in the preformed BiOX is limited [102]. Thus, BiOX with ultrathin 2D structure will be prepared before introducing vacancies by other methods, which is conducive to the uniform distribution of vacancies in the photocatalysts. However, for some bottom-up synthesis approaches, bulk vacancies which can annihilate electrons as deep traps may be induced. Compared with bulk vacancies, surface/subsurface vacancies promote the separation of e^--h^+ pairs, as the carriers at the surface or shallow traps are available for photocatalytic reaction. The formation of ultrathin 2D structure may contribute to

Table 1
Summary of synthetic methods for preparation of vacancy-mediated BiOX.

Method		Processing agents	Processing temperature (°C)	Merits	Demerits	Refs.
Top-down	Light irradiation	High-energy UV light irradiation (inert gas blowing is beneficial)	Room temp	Controllable vacancy concentration	Extra energy employment	[55,56]
	Reduction method	Chemical reductant or electricity	Room temp	Low cost; Simple operation; Controllable vacancy concentration	Introduction of extra impurities	[62,65]
	Thermal treatment	Oxygen deficient or air environment	150–550	Convenient; Controllable vacancy concentration	Extra energy employment	[60,69,71]
	Ultrasound treatment	Ultrasound device	Room temp	Controllable vacancy concentration	Extra energy employment	[75–77]
Bottom-up	Hydrothermal (Solvothermal)	Reducing environment	110–180	Simple operation process	Uncontrollable vacancy type and concentration	[78,79]
	Morphology control	Hydrothermal (solvothermal) conditions and surfactant or reactive ionic liquid	110–180 or Room temp	Controllable crystal morphology	Strict synthesis conditions	[44,87,89]
	Doping method	Ions doping	150–160	Synergistic effect	Introduction of extra impurities	[94,96]
	Hydrolysis	pH regulator or reducing substances	Room temp	Low cost, easy operation	Limited application	[98,99]
	SCS method	Combustible solution	300	Efficient	Complex operation	[100,101]

avoid the generation of bulk vacancies and their negative effects. In a word, morphology control is very important in the process of vacancy formation, so the process of vacancy formation is often accompanied by 2D engineering.

3. Characterization of vacancies

To guide the vacancy engineering for BiOX-based photocatalysis, the formation of vacancies must be recognized and their concentrations should be determined to establish the concentration-activity relationship of vacancy. Up to now, various characterization means have been established to distinguish and understand the vacancies on BiOX. Herein, we classified the existing methods into spectroscopic characterization, microscopic characterization, and computational characterization to introduce.

3.1. Spectroscopic characterization

Spectroscopic techniques are integral to clarify the detailed atomic structures of vacancies on BiOX. X-ray photoelectron spectroscopy (XPS) is a widely adopted technique for ascertaining vacancies on BiOX [103,104]. The existence of vacancies can influence the binding energy and valence state of BiOX elements, resulting in the appearance of a new XPS peak or the shift of peak position. The formation of OVs on BiOX causes a reduction of Bi^{3+} to lower charge $Bi^{(3-x)+}$, which can be reflected by the XPS spectra as the shift of Bi 4f binding energy toward lower binding energy [54,55,78,105-107]. Moreover, it is observed that the appearance of $Bi^{(3-x)+}$ induces two additional peaks [55,78,105,107]. For example, Fig. 5a shows that the Bi 4f spectrum of "perfect" BiOBr/BiOI displays two peaks at 165.1 and 159.7 eV, which can be ascribed to the Bi^{3+} in BiOBr. Compared with "perfect" BiOBr/BiOI, oxygen-deficient BiOBr/BiOI exhibits a ~1.1 eV shift to lower binding energy and two new peaks at 161.7 and 156.3 eV [105]. In contrast to OVs, the introduction of IVs causes the Bi 4f peaks to move to a higher binding energy, because the introduction of IVs inevitably leads to the substitution of a portion of I atoms by O atoms, which enhances the interaction between O^{2-} and Bi^{3+} [37,71,84]. Furthermore, the vacancies formed by the escape of atoms change the atomic ratio of BiOX, which can be determined by XPS test. Thus, the formation of vacancies can be further proved by comparing the relative atomic ratio of BiOX. For example, Cui et al. calculated from XPS test results that the Bi/I value of BiOI increased from 1.5 to 4.8 after calcination, thus confirming that a part of I atoms was lost and abundant IVs were produced during calcination [37]. Some researchers even use XPS as a semi-quantitative method to determine the relative concentration of vacancies by comparing relative atomic ratios [108]. However, given the limited penetration depth of XPS, it can only solve the surface atomic ratio. Furthermore, it must be admitted that there are many factors that can cause the variation of peak position or generation of new peaks in XPS spectra. Therefore, the determination of vacancy generation should be combined with atomic ratio analysis or other characterization methods.

Synchrotron radiation-based X-ray absorption fine structure (XAFS) spectroscopies, including extended X-ray absorption fine structure (EXAFS) spectroscopy and X-ray absorption near-edge structure (XANES) spectra, are important techniques for investigating the local atomic arrangements of BiOX vacancies. The formation of vacancies give rise to changes in the coordination numbers and valence state, resulting in the variation of spectrum [109,110]. The formation of OVs reduces the number of O atoms coordinated with Bi atoms and weakens the oscillation curve peak intensity of Bi-O peak in EXAFS spectroscopy. Meanwhile, the distortion of surrounding atoms caused by OVs can also be reflected by changes of bond lengths in the EXAFS spectroscopy. As a typical example, Fig. 5b exhibits the Fourier transform spectra of the Bi L3-edge EXAFS oscillations of BiOCl with different OVs concentrations [111]. Two sharp peaks around 3.7 Å and 1.8 Å are ascribed to Bi-Bi and Bi-O, respectively. The increase of OVs concentration successively decreases Bi-O peak intensities of OV-1, OV-2 and OV-3. Besides, OVs-induced atomic distortion is reflected as the changes of Bi-Bi and Bi-O lengths which are shortened by 0.13–0.15 Å and 0.02–0.03 Å, respectively. The formation of vacancies can alter the local electronic structures, which can also be observed by XANES spectrum. For example, the formation of OVs in BiOBr atomic layers leads to the appearance of extra peak centered at 529.1 eV in O K-edge XANES spectra (Fig. 5c) [112]. Furthermore, quantitative information of vacancies can be obtained by fitting the data of XAFS to theoretical standards [113]. For example, Zhao et al. [114] obtained the average oxidation state of Ti in bulk TiO_2 and X%-TiO_2 by analyzing the normalized Ti K-edge XANES spectra and Ti K-edge energies. Then, oxygen content and OVs concentration were calculated. Specifically, they revealed that when the content of Cu dopant increased from 0% to 6%, the OVs concentration increased from 0.985% to 8.621%. However, the detailed analysis

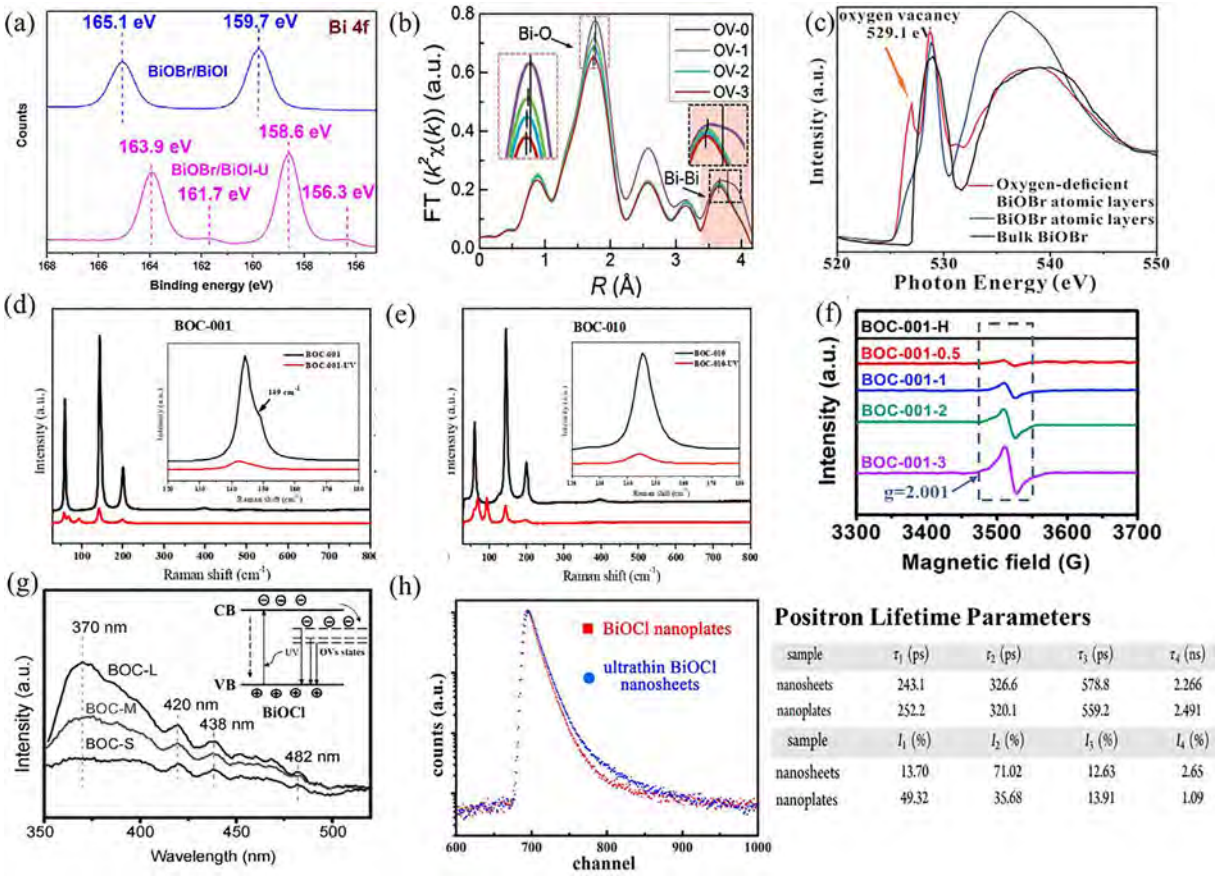

Fig. 5. (a) XPS patterns of Bi 4f for BiOBr/BiOI and BiOBr/BiOI-U. Reproduced with permission [105]. Copyright 2018, Elsevier. (b) Fourier transform spectra of the Bi L3-edge EXAFS oscillations of BiOCl with different OVs concentrations (OV-1, OV-2 and OV-3 possess the lowest, medium, and highest OV concentrations, respectively). Reproduced with permission [111]. Copyright 2018, Elsevier. (c) O K-edge XANES spectra for oxygen-deficient BiOBr atomic layers, BiOBr atomic layers, and bulk BiOBr. Reproduced with permission [112]. Copyright 2018, Wiley. (d) Raman spectra of BOC-001 and UV-irradiated BOC-001-UV samples. (e) Raman spectra of BOC-010 and UV-irradiated BOC-010-UV samples. Reproduced with permission [119]. Copyright 2013, American Chemical Society. (f) EPR spectra of BiOCl samples with different thickness. Reproduced with permission [57]. Copyright 2014, Royal Society of Chemistry. (g) PL emission spectra of as-prepared BiOCl samples. Reproduced with permission [46]. Copyright 2015, Wiley. (insert: The model of the photo-induced electrons and hole excitation–recombination process of BiOCl with OVs. Reproduced with permission [56]. Copyright 2011, Royal Society of Chemistry.) (h) Positron lifetime spectra and the corresponding positron lifetime parameters of BiOCl ultrathin nanosheets and BiOCl nanoplates as well as the calculated positron lifetime values of BiOCl samples. Reproduced with permission [44]. Copyright 2013, American Chemical Society.

of XAFS data in the vacancy-mediated BiOX is absent. Therefore, future research on vacancy-mediated BiOX should pay attention to the quantitative analysis of vacancies by analyzing the XAFS data, so as to explore the role of vacancies at the atomic levels in depth.

Raman spectra is always applied to examine the vibrational and structural properties of BiOX due to their sensitivity to the short-range lattice distortion [111]. The generation of vacancies can alter the vibration mode of a chemical bond, resulting in peak changes [115]. Ordinarily, the formation of OVs leads to the disappearance of B1g band (resulting from the motion of oxygen atoms) round 396 cm^{-1} and emergence of two additional peaks at around 69 and 98 cm^{-1} in Raman spectra, and the intensity of new bands can reflect the relative amount of OVs [42,57,111,116–118]. These two new peaks can be ascribed to the Eg and A1g first-order vibration modes of Bi metal, demonstrating the reduction of Bi^{3+} owning to the introduction of OVs [119]. Besides, the introduction of BiVs will also cause the similar changes. Zhang et al. indicated that the generation of BiVs on BiOCl resulted in the emergence of a new peak at 99 cm^{-1} (the First-order scattering Eg and A1g modes of Bi) as well as disappearance of a peak at 198 cm^{-1} (internal Eg Bi-Cl stretching) [46]. The introduction of vacancies will also induce slight structural distortion, leading to a red shift of Raman spectrum [57,67,99,120]. In addition, if the formation of vacancies weakens the crystallinity of BiOX, the intensity of Raman peaks will decrease [57,99,121]. Zhao et al. introduced OVs on BiOCl-010 and BiOCl-001 by UV light irradiation, and Raman spectroscopy was applied to check OVs generation (Fig. 5d-e) [119]. The Raman spectra of BiOCl-010 and BiOCl-001 exhibit similar changes after UV irradiation: the band at 396 cm^{-1} ascribed to oxygen atoms vanishes and new bands induced by first-order vibration modes Eg and A1g of Bi metal appear (new bands of BiOCl-001-UV appear at 94 and 69 cm^{-1}, and similarly, new bands of BiOCl-010-UV emerge at 95 and 70 cm^{-1}). Besides, the red shift of Raman peaks and the reduction of peaks intensity caused by OVs can also be observed in Fig. 5d-e.

The electron paramagnetic resonance (EPR) technique is the most common and effective method for detecting vacancies in material science. The EPR can provide valuable fingerprinting information about the unpaired electrons [115]. Thus, EPR spectra is regarded as the direct evidence of single-electron-trapped vacancy formation, and the presented different g values and signal intensities indicate defect types and relative concentrations, respectively. For example, the remarkable symmetric peaks at g ≈ 2.001 are typical oxygen vacancy-associated peaks, peaks at g ≈ 3.0 corresponds to the signal of iodine vacancies, and peaks at

$g \approx 2.1$ has been reported to be the surface bismuth vacancies [73,86,112]. Li et al. adopted the EPR method to confirm the formation of OVs on the {001} facets of BiOCl nanosheets and analyze the relative concentration of OVs [57]. The as-prepared samples were named as BOC-001-x (x = 0.5, 1, 2, and 3, which means the millimole quantities of the bismuth precursor). As exemplified in Fig. 5f, all BOC-001-x exhibit a typical signal at g = 2.001 and the intensity increases continuously from BOC-001–0.5 to BOC-001–3, confirming that OVs are successfully introduced and the increase of bismuth precursor concentration is conducive to the formation of OVs.

The photoluminescence (PL) emission spectrum is an auxiliary mean to verify the existence of vacancies in BiOX [46,122,123]. As the trapping centers of photogenerated carriers, vacancies will lead to the formation of new PL emission peaks at larger wavelengths. For instance, the PL spectra of the synthesized BiOCl samples with different thickness are exhibited in Fig. 5g. The dominant ultraviolet-blue emission at around 370 nm can be ascribed to the recombination of free electrons from the CB bottom with the holes at the ground state, corresponding to ~3.44 eV in phonon energy [46]. The recombination of electrons in the vacancy states with photoexcited holes at ground state will generate new photoluminescence at longer wavelengths (insert of Fig. 5g), so those discontinuous visible emissions at ~410–500 nm can be ascribed to the existence of vacancies in BiOCl crystals. Evidently, the emission peaks of BOC-S and BOC-M samples at ~370 nm are weaker than that of BOC-L samples, but other peaks have no obvious change. This phenomenon indicates that there are more vacancy defects in the BOC-S and BOC-M samples leading to the suppressed recombination of free electrons at the ground state [46]. Besides, Deng et al. prepared a series of BiOCl-based materials which exhibited two PL emission peaks centered at 451.5 and 469.4 nm [122]. The 451.5 nm PL emission peak can be attributed to the recombination of photoexcited electrons with valence band holes. The PL emission peak at 469.4 nm confirms the formation of OVs. The appearance of new peak at larger wavelength indicates that the OVs can serve as the trapping centers of photogenerated electrons, thus facilitating the separation of photogenerated carriers.

The positron annihilation lifetime spectroscopy (PALS) is a well-established technique to obtain vacancy type and relative quantity information by measuring the positron lifetime (τ) [124]. PALS can reveal the positron lifetime components (τ) and their relative intensities (I). The τ values reflect the type of vacancies by contrasting them with theoretically calculated positron lifetime. Generally, a larger τ value indicates the formation of larger vacancies, because larger-sized vacancies with lower average electron density can reduce the annihilation rate and increase the positron lifetime [125]. In addition, the relative intensities (I) can determine the relative concentration of various vacancies. For instance, Xie et al. applied PALS to investigate the vacancies in BiOCl nanoplates and BiOCl ultrathin nanosheets [44]. Four lifetime components can be observed from their yielded positron lifetime spectra (Fig. 5h). The two longer-lifetime components τ3 and τ4 can be attributed to positron annihilation in the large defect clusters and the interface, respectively, whereas the shorter ones τ1 and τ2 can be ascribed to the single isolated BiVs and triple Bi^{3+}−oxygen vacancy associates ($V_{Bi}'''V_O^{\bullet\bullet}V_{Bi}'''$), respectively. Besides, the relative intensities (I_1 and I_2) of τ1 and τ2 in these two samples are different, which indicates that isolated BiVs are the major defect in BiOCl nanoplates, but $V_{Bi}'''V_O^{\bullet\bullet}V_{Bi}'''$ are predominant in BiOCl ultrathin nanosheets.

X-Ray Scattering and Pair Distribution Function (PDF) Analysis is a potentially powerful technique that can be applied to quantitatively detect vacancies in BiOX, although it has not yet been used in studies of vacancy-mediated BiOX [126]. The X-ray PDF analysis can reveal reliable atomic–atomic distances of full range. The r value of each peak in PDF function refers to different interatomic distances, and the peak area reflect the relative number of those distance. Therefore, the changes of peaks can accurately provide the structure variation nearby the vacancies. Besides, more detailed information of vacancies can be acquired by fitting the experimental data with a model. For example, Ma et al. assessed the concentration of Ti vacancies by analyzing the real-space refinement of PDF data and fitting individual peaks [127]. The refinement of the Ti rate occupancy (Fig. 6a) shows that the concentration of Ti vacancies decreases with the increase of synthesis temperature. Furthermore, because the PDF peak intensity is related to the atomic density, the specific vacancy concentration can be inferred by comparing the peak intensity relative to a stoichiometric sample. By using the first peak intensity (Fig. 6b, Ti-O/F(OH) bond length), they determined that the Ti occupancy of the samples synthesized at 130, 110, and 90 ℃ are 87, 79, and 69%, respectively. Fig. 6c shows a good agreement between the real-space refinement and peak fitting for high vacancy content assessment, and they further expect that peak fitting is more accurate for materials with low vacancy concentration.

3.2. Microscopic characterization

Microscopic characterization is the most direct way to observe vacancies, which can assist scholars to observe vacancies intuitively. Generally, the scanning transmission electron microscopy (STEM) measurement is a powerful tool for surveying interface microstructure and vacancy defect structure of BiOX. STEM images show that the electronic signal intensity proportional to the atomic number Z fluctuates with the scanning position. For instance, the sharp brightness contrast in the Fig. 7a enables the identification of the Br (Z = 35), I (Z = 53), and Bi (Z = 83) ions [96]. Besides, when the electron beam sweeps on the atomic array, the detector will receive high angle scattered electrons and display bright spots. However, when the electron beam sweeps through the gap between the atomic rows, there are few scattered electrons received, which will form dark spots. Thus, according to the observed relative atomic brightness and the arrangement of atoms in the crystal, vacancy defects can be identified. As a typical example, Fig. 7b-c displays the high-angle annular dark-field scanning transmission electron microscopy (HAADF − STEM) images of V_{Bi}-BiOBr ultrathin nanosheets and BiOBr nanosheets [87]. Compared with Fig. 7b and Fig. 7c, the absence of bismuth atoms on the surface of V_{Bi}-BiOBr ultrathin nanosheets is obvious, which reveals the generation of BiVs. However, the loss of light atoms is difficult to observe from the STEM image. For instance, Zeng et al. found that neither oxygen atoms nor OVs are visible on the annular dark field scanning transmission electron microscopy (ADF-STEM) images which are dominated by Bi and I atom sites, because O (Z = 8) is much lighter than Bi (Z = 83) and I (Z = 53) [128].

3.3. Computational characterization

In addition to traditional instrumental characterizations, theoretical computational approaches, especially the density functional theory (DFT) calculation, are indispensable means to furnish insightful information for vacancies research. DFT calculation can accurately predict the formation energy of vacancies in BiOX from a theoretical point of view, explain the internal mechanism of vacancy formation, and guide the design of suitable vacancy-mediated materials. For instance, based on the DFT computation, Alvarez et al. calculated the formation energy of BiVs in different types of BiOCl nanosheets (Fig. 7d-f) and found that BiVs should be more energetically favorable for BiOCl nanosheets with pores

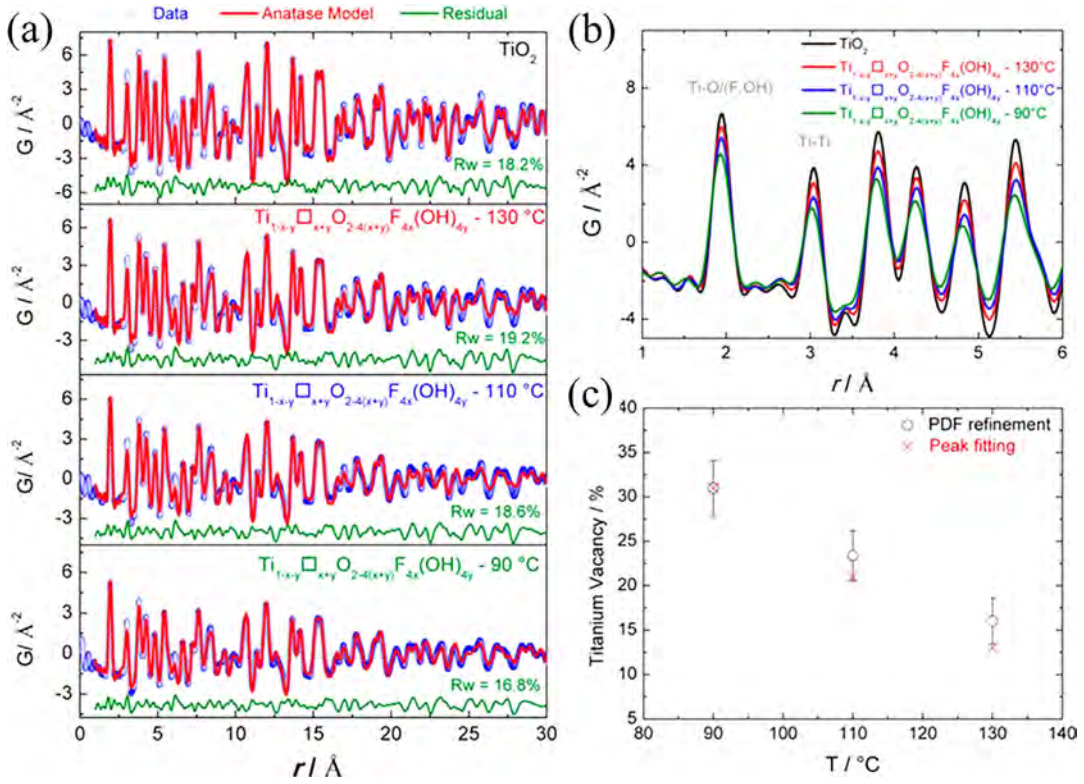

Fig. 6. (a) PDF refinements of anatase TiO_2 and $Ti_{1-x-y}\square_{x+y}O_{2-4(x+y)}F_{4x}(OH)_{4y}$ prepared at 90, 110, and 130 °C. (b) Zoom on the short-range order of PDF data for anatase samples. (c) Determination of the titanium vacancy concentration using real-space refinement and peak fitting for anatase samples. Reproduced with permission [127]. Copyright 2018, American Chemical Society.

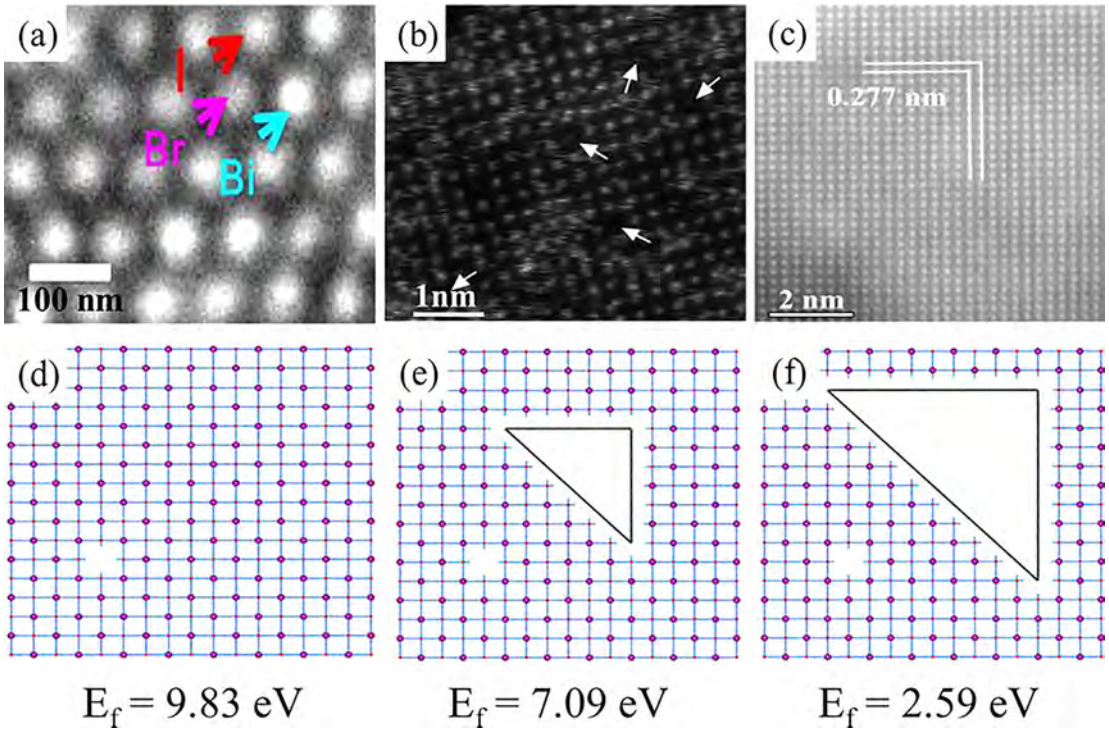

Fig. 7. (a) Magnified HAADF-STEM image of the $BiOBr_{0.75}I_{0.25}$ shell along with [0 1 0] direction. Reproduced with permission [96]. Copyright 2016, American Chemical Society. Aberration-corrected HAADF-STEM images of V_{Bi}-BiOBr UNs (b) and BiOBr nanosheets (c). Reproduced with permission [87]. Copyright 2019, American Chemical Society. The formation energy (Ef) of BiVs in different types of BiOCl nanosheets, including a 9 nm^2 nanosheet without pores (d), a 9 nm^2 nanosheet with a 0.83 nm^2 pore (e), and a 9 nm^2 nanosheet with a 2.86 nm^2 pore (f). A smaller Ef value indicates a higher likelihood of Bi vacancy formation. Reproduced with permission [125]. Copyright 2018, American Chemical Society.

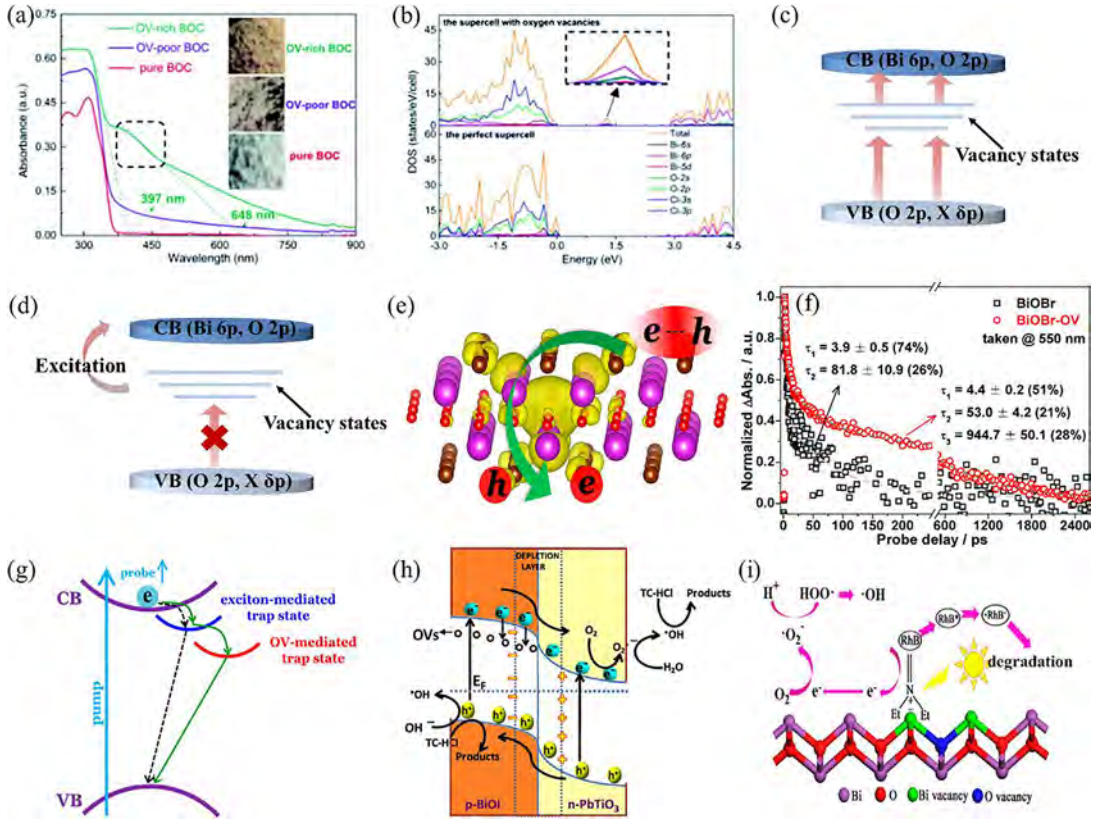

Fig. 8. (a) UV–vis diffuse reflectance spectra of BiOCl samples. (b) DOS of pure BiOCl and BiOCl with OVs. Reproduced with permission [109]. Copyright 2018, Royal Society of Chemistry. The presence of vacancies can optimize electronic band structure by introducing defect levels in the middle of the band gap, which serve as springboard (c), or shows a shallow donor behavior (d). (e) Vacancies can induce exciton dissociation. (f) TA kinetic traces probed at 550 nm for BiOBr and BiOBr-OV. (g) Schematic illustration of the photophysical processes involving exciton- and oxygen-vacancy-mediated trap states. Reproduced with permission. Reproduced with permission [67]. Copyright 2018, American Chemical Society. Vacancies can promote photoexcited carriers separation by boosting charge carriers mobility across the heterojunction boundary (h). Reproduced with permission [141]. Copyright 2019, American Chemical Society. Schematic diagram illustrating the absorption and degradation of positively charged RhB molecules by BiOCl with negative vacancy associate (i). Reproduced with permission [44]. Copyright 2013, American Chemical Society.

[125]. Based on DFT results, they put forward a new mechanism for inducing vacancy generation: the existence of mesopores helps to reduce the formation energy of vacancies, because the existence of mesopores will cause thermodynamic instability of the system which can be counterbalanced by generating vacancies nearby.

4. Roles of vacancy in regulating photocatalytic behavior of BiOX

Given that numerous efforts have been devoted to improving the photocatalytic activity of BiOX through vacancy engineering, it is vital to penetrate deeply into critical actions of vacancies on photocatalysis. Herein, we summarize the positive roles of vacancies in regulating each step of BiOX photocatalytic behavior, which grants clear understanding for researchers to further effectively customize various vacancies in BiOX and even other photocatalysts for performance optimization.

4.1. Band structure regulation

Once atoms are removed from the lattice position, the atoms around the vacancy induce changes in the chemical environment, such as electron redistribution. Even if the vacancy concentration is very low, it can affect the band structure of the new structure [52,129,130].

Usually, oxygen vacancies tend to form intra-band gap states, causing the enhancement of light absorption and red shift of optical response range of BiOX [45,107]. Taking BiOCl as an example, its band gap is about 3.2 eV, which makes it inactive under visible light [109,131]. After creating rich OVs in BiOCl, UV–vis diffuse-reflectance spectroscopy (Fig. 8a) displays that the tail extends to the visible light region, which can be ascribed to the electronic states located in the band gap [109]. The calculated density of states confirms that new electronic states are generated by the hybridization of occupied Cl-3p, O-2p, and Bi-6p orbitals (Fig. 8b). The intermediate defect levels can not only serve as springboards to facilitate the excitation of charges from VB to CB, leading to the intensified light absorption (Fig. 8c) [132,133], but also show a shallow donor behavior, suggesting that local electrons may be excited to CB of BiOX with the illumination of low energy light (Fig. 8d) [57]. At the same time, OVs are also considered to change the positions of VB maximum (VBM) and CB minimum (CBM) [89,109,134]. For example, Cui et al. concluded that BiOCl with small amount of OVs has no intermediate electronic states, but its CB and VB have a positive shift. When the content of OVs increases, intermediate energy levels are induced, and both CB and VB shift downward [109]. Furthermore, Xue et al. reported that the formation of OVs causes the VBM of BiOBr nanosheet to move form 1.5 eV to 0.95 eV. Correspondingly, VBM shifts to −1.48 eV from −1.19 eV [89].

The presence of iodine vacancies can directly change the positions of VBM and CBM without new middle states formation. In order to illustrate the influence of IVs on the band structure of BiOI, Wang et al. studied the density of states (DOS) of BiOI, $Bi_8O_8I_6$, and $Bi_8O_8I_4$ by using the standard DFT calculation [73]. $Bi_8O_8I_6$ and Bi_8-

O_8I_4 represent that the content of IVs is 25% and 50%, respectively. They discovered that the band gaps (1.58 eV) of $Bi_8O_8I_6$, and $Bi_8O_8I_4$ are almost identical with that (1.57 eV) of BiOI. However, both the VBM and CBM of $Bi_8O_8I_6$ and $Bi_8O_8I_4$ shift to a more positive energy position compared with BiOI. Therefore, they think that IVs lead to the downward shift of the VBM with no obvious bandgap change. However, the UV – vis absorption spectra reflect that when the vacancy concentration is greater than 34%, the absorption edges show an obvious blue shift, which exhibits a slight deviation from the calculation results. Moreover, some studies reveal that IVs can enlarge the band gap of BiOI. For example, Guan et al. considered that IVs are formed by replacing two iodine atoms with one oxygen atom during the heat treatment (400 ℃ for 5 h), and the chemical formula of the processed sample is determined as $BiO_{1.18}I_{0.64}$ [135]. Then, they calculated that the band-gap energies of BiOI and $BiO_{1.18}I_{0.64}$ are about 1.80 and 2.61 eV, respectively, which are consistent with the results of UV–vis diffuse reflectance spectra. Similarly, Wang et al. prepared BiOI containing IVs by solvothermal method, and its band gap (2.18 eV) is larger than that (1.96 eV) of pristine BiOI [84]. Therefore, it can be concluded that the regulation of IVs on the band structure is closely related to the concentration, incorporating method of IVs and etc.

The regulation of the energy band structure by the bismuth vacancies is manifested in directly narrowing the band gap by adjusting the positions of the VB and CB [85,87]. For example, Di et al. measured the VB of BiOBr nanosheets and BiVs-BiOBr ultrathin nanosheets by the XPS VB spectra, and they found that the VB potential moves from 2.01 eV of BiOBr to 1.57 eV of BiVs-BiOBr [87]. Besides, the band gaps of BiOBr and BiVs-BiOBr are estimated to be 2.77 and 2.65 eV, respectively, from UV–vis diffuse reflection spectra [87].

4.2. Carriers behavior improvement

The generation and migration are main behaviors of carriers involved in the process of photocatalysis. Thus, we mainly discuss the effect of vacancies on carriers behavior from these two perspectives.

The existence of oxygen vacancies can induce exciton dissociation, thus promoting the generation of carriers in photocatalytic system. Exciton, which may be the dominant photogenerated species, can be described as bound e^-–h^+ pairs mediated by Coulomb interaction. Given the competition between charge carriers and excitons in the process of photoexcitation, it is reasonable to obtain desirable quantum yields via dissociating excitons into free electrons and holes. Ma et al. demonstrated that OVs are beneficial to induce exciton dissociation, thereby achieving efficient photocatalytic CO_2 conversion for BiOCl nanosheets [136]. Xie et al. proposed that OVs can effectively promote excitons dissociation into free carriers (Fig. 8e) [67]. DFT calculation clearly states that the localization of the band-edge states near the vacancies is severely distorted by OVs, resulting in the exciton instability [67]. Then, they further verified the robust exciton dissociation mediated by OVs via ultrafast transient absorption spectroscopy. Femtosecond time-resolved transient absorption (TA) kinetic traces detected at 550 nm for both BiOBr and BiOBr-OV are shown in Fig. 8f. Obviously, compared with the BiOBr, the BiOBr-OV displays a longer recovery lifetime of photoinduced electrons. Clearly, TA kinetics of BiOBr is fitted well by the biexponential decay function ($\tau1$ = 3.9 ± 0.5 ps, 74%; $\tau2$ = 81.8 ± 10.9 ps, 26%; average lifetime ~24 ps). The black dotted lines in Fig. 8g can well illustrate the two consecutive relaxation pathways of BiOBr system with robust excitonic effects, where the exciton-mediated trap state serves as an intermediate trap state. For BiOBr-OV, a triexponential decay function process ($\tau1$ = 4.4 ± 0.2 ps, 51%; $\tau2$ = 53.0 ± 4.2 ps, 21%; $\tau3$ = 944.7 ± 50.1 ps, 28%) with an average lifetime of ~278 ps can be observed. The olive solid lines in Fig. 8g illustrate the three-step relaxation pathways. The photoinduced electrons experience a rapid relaxation ($\tau1$) from the CB minimum to the exciton state, then the resulting excitons relax to the OV-mediated trap state and dissociate into free charges simultaneously ($\tau2$), and finally decay on a nanosecond time scale ($\tau3$). The ultrafast TA analyses further highlight the effect of OVs on inducing exciton dissociation. When it comes to the impact of OVs on carriers migration, it can be discussed from the following three aspects. Firstly, OVs act as the capture centers for photoexcited electrons to suppress the recombination of photoexcited carriers, thereby more oxidizing holes and reducing electrons participate in the redox reaction on the surface of BiOX [137-139]. Photogenerated electrons in the CB preferentially transfer to oxygen vacancy states within the middle of band gap rather than recombine with photoexcited holes, leading to photoexcited charge carriers life time extension [42,133,140]. Secondly, the enhanced VB width of OVs-mediated BiOX promotes the migration of holes, and the elevated CBM facilitates the transfer of electrons with higher reduction ability [116,134]. Finally, it is reported that OVs can efficiently tailor charge carriers' mobility across the heterojunction boundary (Fig. 8h) [141–143]. For example, Paramanik et al. believed that in the BiOI/PbTiO3 p-n heterojunction, oxygen vacancy states serve as new channels for photoelectrons to transfer from BiOI to PbTiO, which leads to an effective decrement of the charge recombination [141].

Iodine vacancies can serve as traps for photoexcited holes [37,135]. Besides, because the electronegativity of I atom is lower than that of O atom, the generation of IVs (partial I atoms are replaced by O atoms) leads to the enhancement of the internal electric field of BiOI [135]. Consequently, IVs are generally considered to facilitate the separation of photoinduced electron-hole pairs. Guan et al. calculated that the effective mass of hole is 6.1 times that of electron in BiOI with IVs, while the effective mass of hole is 3.5 times that of electron in BiOI. Therefore, BiOI with IVs has a faster electron-hole relative movement rate compared with BiOI. In addition, Cui et al. investigated the photoelectric properties of BiOI with IVs and pristine BiOI. The transient photocurrent responses shows that BiOI with IVs exhibits much more efficient separation of photogenerated electron-hole pairs than that of pristine BiOI.

For BiOX monomer photocatalyst, carriers migration is closely related to two features: the VB width and the CB minimum energy. The VB width inherently determines the mobility of holes: the wider VB leads to the higher mobility of photoexcited holes [144]. Elevation of the CB minimum energy is also vital, since it facilitates the rapid transfer of photogenerated electrons to reactants [44,145]. As mentioned above, BiVs can regulate the band structure, may leading to the widening of VB width and the upward shift of CB minimum energy. Xu et al. reported that the shallow bismuth-vacancy states locate above the VB and partially overlap the VB of BiOCl. This not only narrows the band gap, but also increases the width of VB. The wider VB suggests the higher mobility of photogenerated holes. Besides, the CBM of BiVs-mediated BiOCl also has a certain enhancement. Therefore, BiVs endow BiOCl with high carriers transfer efficiency [85].

4.3. Surface properties changes

Surface properties are vital for the photocatalytic performance of BiOX. Surface OVs can serve as active sites to directly participate in the photocatalytic reactions by building strong interaction with target molecules. Specifically, surface OVs due to its electron donor nature may perform as active sites to promote the adsorption, activation or dissociation of substrate, thereby enhancing the surface reaction rates of BiOX. As for CO_2 reduction process, Ren et al.

revealed that surface OVs on BiOBr can absorb CO_2 with monodentate and bidentate mode, followed by turning it into lattice oxygen, thus triggering the reduction of CO_2 [146]. This reflects that the OVs shows excellent CO_2 affinity and activation ability. In addition, OVs can serve as N_2 adsorption and activation sites. Temperature-programmed desorption of N_2 experiments found that BiOBr with OVs began to show a single N_2 desorption peak at 176 °C with the center at 265 °C, which was associated with the chemical adsorbed N_2 [45]. However, there was no N_2 adsorption on perfect BiOBr. This difference proved that OVs are indispensable for N_2 adsorption. Then, Li et al. traced the electrons transfer behavior and revealed that OVs can donate their localized electrons to the π N-N antibonding system to activate the $-N_2$ ligand [45]. The N–N bond length of N_2 was prolonged to 1.133 Å over the OVs in (001) facet exposed BiOBr. This bond length is between the triple bond length (1.078 Å) of free molecular nitrogen and the double bond length (1.201 Å) of diazene, which further reflected the effective activation of N_2. A typical example for the effect of vacancies on substrate dissociation is that the OVs of BiOCl with electron donor nature can perform as "Fenton-catalytic" centers to dissociate H_2O_2 into •OH [117]. OVs on the BiOCl back donate sufficient charges to the absorbed H_2O_2, leading to the spontaneous dissociation of H_2O_2 in the manner of Fenton reaction toward the generation of a free •OH and a OH^- bound on the OV [117]. Moreover, vacancy associate has also been reported to alter the surface properties of BiOX by providing abundant extraordinary electrons. Guan et al. stated that the $V''_{Bi}V^{\bullet\bullet}_{O}V_{Bi}''$ vacancy associate associated with four negative charges favors the adsorption of positively charged substrate molecules (such as Rhodamine B and Methyl Orange) (Fig. 8i) [44].

4.4. Molecular oxygen activation

Photocatalytic process can activate molecular oxygen (O_2) to produce reactive oxygen species (ROS) like $\cdot O_2^-$, ·OH, and H_2O_2. These ROS with excellent oxidation capacity have good performance on decomposing organic pollutants and other applications. Thus, the improvement of photocatalytic activity of BiOX is closely related to the activation level of molecular oxygen. However, the weak interaction between O_2 and the intact BiOX surface leads to a tardy activation kinetics of O_2. Fortunately, it is found that oxygen vacancies on semiconductors surface can furnish coordinatively unsaturated sites for O_2 activation in photocatalytic process [57,119,147]. Therefore, O_2, which is theoretically impossible to absorb on the clean surface of BiOX, can be absorbed on the surface of BiOX with the existence of OVs [119,148]. Besides, as mentioned above, the existence of OVs can improve the behavior of photogenerated carriers, so that more charge carriers can arrive at the molecular oxygen absorbed on BiOX to promote the activation of molecular oxygen.

Vacancies not only promote the activation level of molecular oxygen, but also has great influence on the activation state ($\cdot O_2^-$, O_2^{2-} or $^1O_2$) of molecular oxygen depending on the structure and type of the vacancy. It is reported that $\cdot O_2^-$ is generated via one-electron reduction, while O_2^{2-} is produced by two-electron reduction. The specific process of photogenerated electron transfer depends on the first step of continuous reactions on the semiconductor surface. Besides, the emergence of $^1O_2$ can be attributed to the energy transfer process. Since vacancies are formed by the disappearance of atoms, it is generally believed that the structure of vacancies is determined by the geometric atom arrangement around them [119,149]. Therefore, the regulation of OVs structure is realized by changing the surrounding atoms. Introducing OVs into different crystal faces, due to its easy operation, become the most commonly used method to control the OVs structure, thereby the OVs structure often classified by crystal faces. For example, different structure of surface OVs can be introduced on the (001) and (010) surface of BiOCl, owning to their different surface atom exposure. The OVs generated on the (001) plane with a closely packed O-exposed structure can be named as OVs-001, while the OVs-010 formed on the (010) plane with an open channel structure exposed with Bi, Cl, and O atoms [119]. The structure of surface OVs further affects the adsorption mode of O_2 on OVs. Molecular oxygen is attached to an OVs-001 site in an end-on structure by connecting two nearby Bi atoms in the sublayers (Fig. 9a), then O_2 can extract one electron from redistributed surface charges to produce $\cdot O_2^-$ species (Fig. 9c) [119]. However, O_2 connects with the OVs-010 in a complex bridge-on structure by connecting two nearest Bi atoms in outer layer and one next nearest Bi atom in sublayer (Fig. 9b), which favors the simultaneous transfer of two electrons to connected O_2 and produces O_2^{2-} (Fig. 9c) [119]. Furthermore, the activation state of molecular oxygen can also be modulated by the vacancy type. Generally, larger vacancy clusters with longer positron lifetimes favor the generation of $^1O_2$. Because large vacancy clusters distributed in the depth of BiOX tend to localize the excited electrons, and therefore impede the transfer of electrons between the BiOX and the surface adsorbate. This situation facilitates the generation of $^1O_2$, whose generation only involves energy transfer between BiOX and absorbed O_2, for its competing reactions for generating $\cdot O_2^-$ correlated with electron transfer are automatically suppressed. For example, Chen et al. reported that $V^{\bullet}_{Br}V^{\bullet\bullet}_{O}V_{Bi}''$ triple atom vacancy cluster (with positron lifetime 289.9 ps) is beneficial for the generation of $^1O_2$, while V_{Bi}'' $V^{\bullet\bullet}_{O}$ vacancy cluster (with positron lifetime 241.7 ps) is facilitating the production of $\cdot O_2^-$ [147]. Furthermore, they proved that $V^{\bullet}_{Br}V^{\bullet\bullet}_{O}V_{Bi}''$ triple atom vacancy can effectively reduce the singlet–triplet energy gap and promote intersystem-crossing, thus promoting the production of $^1O_2$ related to the energy transfer process [147].

As mentioned above, the introduction of vacancies can easily achieve enhanced photocatalytic activity for BiOX. However, vacancies do not always bring good impacts, depending on the vacancies location and quantity [46,47]. For example, Xia et al. reported that the photocatalytic performance of RhB degradation was weakened by high OVs concentration [150]. Besides, it is generally agreed that bulk vacancies may act as the carrier trapping and recombination sites, which will bring negative effects on photocatalytic performance, while surface and subsurface vacancies are conducive to the separation of photoinduced carrier because the charges captured on surface or shallow traps are available for photocatalytic reactions [151]. Moreover, vacancies also suffer from the disadvantage of instability [42]. Therefore, in order to better play the positive roles of vacancies, the comprehensive design of vacancies through calculation and other methods is essential, and the role of vacancies should be further evaluated.

5. Vacancy engineered BiOX for various photocatalysis applications

As previously described, vacancy design can adjust the electronic structure, carrier migration, and interface redox reaction, which contribute to enormous potential to improve the photocatalytic activity of BiOX. In this section, the behavior of vacancies and the resulting advanced photocatalytic performance on pollutants removal, water splitting, CO_2 reduction, nitrogen fixation, and selective oxidiation are discussed in detail (Table 2).

5.1. Pollutant removal

Vacancy engineering is widely used to improve the performance of bismuth halide for pollutant removal. BiOX with vacan-

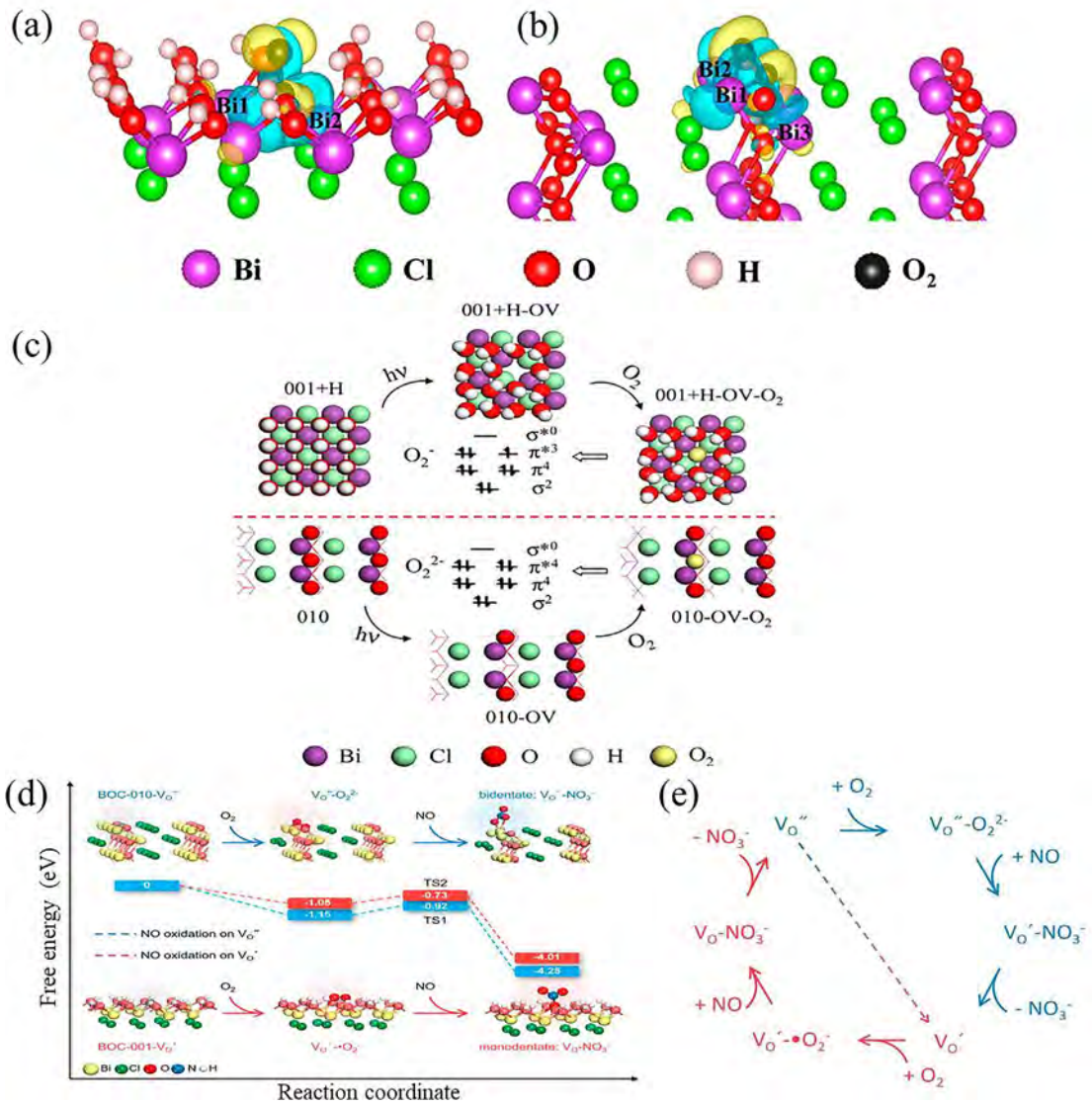

Fig. 9. (a) O_2 absorb on (001) surface of BiOCl via an end-on structure. (b) O_2 absorb on (010) surface of BiOCl via a bridge-on structure. (c) Molecular oxygen activation processes on BiOCl (001) surface and BiOCl (010) surface. Reproduced with permission [119]. Copyright 2013, American Chemical Society. (d) Free energy change during O_2^{2-} and $\bullet O_2^-$-mediated NO oxidation on the OVs of BOC-010 and BOC-001, respectively. (e) Proposed NO oxidation on the $V_O^{\cdot}$ of BOC-010. Reproduced with permission [167]. Copyright 2019, American Chemical Society.

cies can not only effectively remove pollutants (dyes, antibiotics, endocrine disruptors, etc) in water body, but also achieve efficient air purification [152-159]. Even for the degradation of some special pollutants, vacancies play a critical role. For example, perfluorooctanoic acid (PFOA), an emerging persistent organic pollutant, is resistant to the oxidation of ·OH [160,161]. However, photogenerated h^+ has been demonstrated to be able to degrade PFOA even under harsh conditions. Therefore, in the process of photocatalytic degradation of PFOA, it is vital to retard the recombination of photoinduced e^--h^+ pairs, suppress the conversion of holes to ·OH, and enhance the ability of hole oxidation. The introduction of OVs greatly meets above requirements, thus realizing the degradation of BiOCl on PFOA [83,98,160]. Furthermore, OVs mediated BiOBr shows enhanced nonselective photocatalytic performance for remediating oil field produced wastewater (OFPW) [162]. The chemical oxygen demand value of OFPW can be reduced from 18,900 to 6800 mg·L^{-1} after 5 h photocatalytic treatment with OVs-mediated BiOBr, and the COD reduction rate is twice as high as that of pure BiOBr [162].

The air purification function of vacancy engineered BiOX is mainly manifested by the degradation of formaldehyde (HCHO) and the oxidation of nitric oxide (NO) [134,163,164]. Tong's group successfully introduced OVs into BiOI by using ultrasound, doping and low concentration nitric acid assisted methods [76,103,134]. Under visible light illumination, the BiOI with OVs can effectively convert the HCHO into CO_2 and H_2O, and more than 99% HCHO can be removed within 2 h, which is three times higher than that of perfect BiOI [76]. Furthermore, Tong et al. also found that introducing OVs can enhance the stability of BiOI for HCHO oxidation [134]. Normally, the deposition of carbonaceous intermediates during the degradation of formaldehyde will lead to the deactivation of photocatalyst, while the existence of OVs can effectively facilitate the charge migration to produce more ROS for avoiding the deposition of intermediates [134]. Tong et al. proposed that oxygen-deficient BiOI can generate more ROS during the degradation process, thereby maintaining the photocatalytic activity. Anthropogenically derived NO, even at tiny concentration (subppm or ppb levels), is still considered to cause great harm to human

Table 2
Recent studies on vacancy-mediated BiOX for various photocatalytic applications.

Photocatalysts	Vacancy types	Vacancy creating approaches	Reaction conditions	Photocatalytic activity of the vacancy-mediated photocatalysts (the vacancy-free counterparts)
BiOCl nanosheets [44]	$V_{Bi}'''V_O^{\bullet\bullet}V_{Bi}'''$	2D engineering	5 mg Photocatalyst dispersed in 100 mLof 10^{-5}M RhB solution, 150 W Xe lamp	98% (less than 20%) of RhB are degraded after 20 min
BiOCl [99]	Dual-vacancies of O and Cl	Hydrolysis method	50 mg of photocatalyst dispersed in 50 mL of 0.1 mM RhB solution, 500 W Xe lamp (λ > 400 nm)	77.7% (36.6%) of RhB are degraded after 5 h
BiOI [73]	IVs	Thermal treatment	50 mg of photocatalyst dispersed in 100 mL of 0.02 mmol/L phenol, a solar simulator of 300 W	Almost all the phenol is degraded in 4 h (no obvious photodegradation activity)
BiOI thin films [37]	IVs	Thermal treatment	Glass plate with I-deficient BiOI film was hung in the tube containing 40 mL of 10 mg L^{-1} BPA, 800 W xenon lamp	Almost all BPA are degraded in 30 min (only 75% of BPA are degraded in 60 min)
BiOI nanosheets [54]	OVs	Electroreduction strategy	15 mg Photocatalyst dispersed in 100 mL of 10 mg/L MO solution, 500 W Xe lamp with a 420 nm cutoff filter	more than 99.1% (48.8%) of MO are degraded after 120 min
BiOI nanosheets [76]	OVs	Ultrasound treatment	100 mg Photocatalyst, 500 ppm HCHO, 100 W tungsten halogen lamp with a 420 nm cutoff filter	more than 99% (35%) of HCHO are degraded after 120 min
BiOCl [163]	OVs	Solvothermal reduction treatment	Prepared BiOCl films, 500 ppb NO gas with a flow rate at 1 L/min, a xenon lamp (λ > 400 nm)	70% NO removal with selectivity exceeding 99% within 15 min (could not remove NO efficiently)
BiOBr/BiOI [105]	OVs	2D engineering	glass dish coated with 0.15 g photocatalyst, 600 ppb NO gas, a Xe lamp (λ > 420 nm)	57% (10%) of NO are removed in 50 min
BiOCl [109]	OVs	Solvothermal reduction treatment	30 mg Photocatalyst dispersed in 30 mL of 0.05 mol/L $AgNO_3$ aqueous solution, 300 W Xe lamp with a 420 nm cutoff filter	344 mmmol/g/h (104 mmmol/g/h) for oxygen evolution
BiOCl [80]	OVs	Solvothermal reduction treatment	50 mg Photocatalysts dispersed in 50 mL of water containing 10 vol% triethanolamine, 300 W xenon lamp with a 420 nm cutoff filter	2.51 mmol/h (0.12 mmol/h) for hydrogen evolution
BiOCl [42]	OVs	Light irradiation method	0.1 g photocatalyst dispersed in 100 mL of deionized water, 400 ppm CO_2 gas, 500 W Xe lamp	8.1 μmol/g (/) for CO_2 reduction to CO in 8 h
BiOBr [107]	OVs	Solvothermal reduction treatment	Glass road coated with photocatalyst, CO_2 pass through the photocatalyst for 30 min at a flowrate of 50 mL/min, 500 W Xenon arc lamp with an AM 1.5 filter	9.58 mmol/g (2.99 mmol/g) for CO_2 reduction to CH_4 over 10 h
BiOBr nanosheets [87]	BiVs	2D engineering	30 mg sample dispersed in 50 mL of pure water, high-purity CO_2 with a pressure of 0.08 MPa pumped into, 300 W Xe lamp	20.1 μmol/g/h (5.3 μmol/g/h) for CO_2 reduction to CO
BiOCl [136]	OVs	Solvothermal reduction treatment	0.05 g photocatalyst dispersed in water with 1.3 g $NaHCO_3$, 10 mL 4 M H_2SO_4 was added 1 to achieve atm CO_2 gas, 300 W Xe lamp	35.03 μmol/g (14.78 μmol/g) for CO_2 reduction to CO in 4 h
BiOBr [112]	OVs	Light irradiation method	0.1 g photocatalyst dispersed in 100 mL water, CO_2 gas bubbled at 0.5 mL/min, 300 W Xe lamp with a 400 nm cutoff filter	87.4 mmol/g/h (around 4.4 mmol/g/h) for CO_2 reduction to CO
BiOBr [45]	OVs	Solvothermal reduction treatment	0.05 g photocatalyst dispersed in 100 mL of double distilled water, high-purity N_2 bubbled at a flow rate of 60 mL/min, 300 W xenon lamp with a 420 nm cutoff filter	104.2 μmol/h/g for NH_3 production(No significant amount of NH_3 is detected)
BiOBr [89]	OVs	2D engineering	50 mg photocatalyst dispersed in 100 mL deionized water, high-purity N_2 bubbling, a 300 W Xe lamp	49.04 μmol/g/h (2.83 μmol/g/h) for NH_3 production
Fe-doped BiOBr [94]	OVs	Doping method	50 mg photocatalyst dispersed in the solution of 100 mL of deionized water, N_2 bubbled at a rate of 60 mL/min, 300 W xenon lamp with a 420 nm cutoff filter	382.68 μmol/g/h (51.68 μmol/g/h) for NH_3 production
BiOCl [79]	OVs	Solvothermal reduction treatment	0.2 g photocatalyst dispersed in 100 mL water, N_2 flow at a rate of 0.3 L/min, Xe lamp (λ greater than 300 nm)	NH_3 is produced (around 6.5 μmol after 3 h) (NH_3 is not produced)
Au nanoparticles-BiOCl [185]	OVs	Solvothermal reduction treatment	50 mh photocatalyst dispersed in 10 mL acetonitrile containing 0.5 mmol benzyl alcohol, O_2 atmosphere, 8 h, 300 W Xe lamp with a 420 nm cutoff filter	Converting benzyl alcohol to benzaldehyde with 75.6% (7.3%) conversion and 99% (93.9%) selectivity
BiOBr [147]	V_{Br}·V_{Bi}"V_O"	Solvothermal reduction treatment	50 mg sample spersed in 10 mL acetonitrile containing thioanisole, 0.1 MPa O_2 atmosphere, 300 W Xe lamp (λ greater than 420 nm)	Converting thioanisole to sulfoxide with 93% (/) conversion and 99% (/) selectivity
BiOCl [111]	OVs	Solvothermal reduction treatment	60 mg photocatalyst dispersed in 5 mL acetonitrile containing 0.05 mmol butylbenzylamine, 1 atm O_2 pressure, 10 h, 300 W Xenon lamp with a 420 nm cutoff filter	Converting butylbenzylamine to N-*tert*-butylbenzylimine with 85% (4%) conversion and 87% (0) selectivity
BiOBr [67]	OVs	Thermal treatment	10 mg photocatalyst dispersed in 1 mL acetonitrile containing 0.2 mmol benzylamine, air atmosphere, 12 h, xenon lamp with a 420 nm cutoff filter	Converting benzylamine to N-benzylidenebenzylamine with 96% (24%) conversion and 99% (95%) selectivity
BiOCl nanosheet [186]	OVs	2D engineering	8 mg photocatalyst dispersed in 1 mL acetonitrile containing 0.2 mmol benzylamine, 1 atm O_2 pressure, 10 h, 300 W Xe arc lamp with a 400 nm cutoff filter	Converting benzylamine to N-benzyleneamine with87.6% (36.9%) conversion and 96.9% (99%) selectivity

health and the environment [165]. Although photocatalytic technology is regarded as a promising technology for NO removal, it is still inevitably subject to the generation of toxic intermediates (NO_2). The generation of undesirable NO_2 is generally ascribed to the existence of one-oxygen reactive species such as •OH and O^-, which will perniciously result in the partial oxidation of NO (NO (g) + O^-/•OH → NO_2(g)) [163]. Fortunately, the introduction of OVs in BiOX can not only promote the oxidation of NO, but also improve the selectivity of oxidation process to inhibit the generation of toxic intermediates [163,166-168]. Zhang's group used

BiOCl (BOC) as the prototypical catalyst to investigate the mechanism of NO selective oxidation mediated by OVs. They found that the distinct geometric structure of OVs, depended on the intrinsic surface atomic structure of BOC-010 and BOC-001, ultimately lead to different mechanisms for selective oxidation of NO. As mentioned earlier, OVs with different structures can generate different oxygen species, which are supposed to be the key to achieve aerobic catalytic NO removal, because O_2 interacted more strongly with OVs than NO according to the activated bond lengths and adsorption energies. An OV on the surface of BOC-010 can form an archetypal F center (V"o") by localizing two electrons, then the adsorbed O_2 can be activated into O_2^{2-} in a side-on bridging state, which further oxidizes NO into bidentate nitrate with a small energy barrier (Fig. 9d) [119,167]. The detailed process can be described as follows (Fig. 9e). Under the illumination of solar light, the NO oxidation on V"o" begins with a two-electron charging process (V"o" + O_2 → V"o"–O_2^{2-}), followed by a discharging process involving one electron (V"o"–O_2^{2-} + NO → Vo′ –NO_3^- + e^-). Then, the OV can recapture the back-donated electron to generate a new single-electron-captured OV (Vo′), simultaneously initiating the second round of NO oxidation to form VO-NO_3^-. While OV on the surface of BOC-001 is intrinsically a Vo′ oxidizing NO by the production of side-on bridging •O_2^- (Fig. 9d) which can directly oxidize NO into monodentate nitrate without any barrier (ΔE = − 3.10 eV)[119,163,167]. Therefore, BOC-001 with OVs can realize 70% NO removal with selectivity exceeding 99% within 15 min visible light illumination. Online monitoring system only detected 4 ppb NO_2, suggesting that most of NO was directly oxidized to nitrate [163].

5.2. Water splitting

Photocatalytic water splitting has been considered to be one of the most promising processes to overcome the depletion of fossil fuels and a series of derivative environmental problems associated with their combustion [169]. Photoexcited electrons can reduce water molecules to generate hydrogen fuels, while photoinduced holes can oxidize water molecules to form O_2 through overall water splitting. The focuses of photocatalytic water splitting are the energy band structure and the interfacial charge transfer behavior. By virtue of abundant surface vacancies, the efficiency of photocatalytic hydrogen production by BiOX can be significantly improved [46,59]. Because these surface vacancies cannot only move both VB and CB upwards but also effectively adsorb and dissociate H_2O molecules as active sites [46]. As for BiOCl, the upward shift of conduction band increases the driving force for water reduction, thus facilitating the migration of photogenerated electrons to H_2O molecules. Meanwhile, the maximum of VB is still more positive than that of O_2 / H_2O (+1.23 ev). Furthermore, the role of OVs as active site was confirmed by DFT calculation. On the pristine BiOCl surface (Fig. 10a), the water molecule dissociates into a H atom bonded with a surface oxygen atom and an OH group bonded with the bismuth site. Then, the OH group overcome a high energy barrier of 3.33 eV to dissociate into O atom, which severely limits the water splitting reaction on the pristine BiOCl surface. However, on the surface of BiOCl with an OV (Fig. 10b), H_2O is dissociated into a bonded H atom and an OH group which can fill the OV and repair the surface. Subsequently, the two H atoms on the repaired BiOCl surface will be dissociated to generate a H_2 molecule owning to the role of entropy. Therefore, when the vacancy-mediated BiOCl is exposed to appropriate light illumination, hydrogen evolution can be more efficient, and water oxidation for oxygen production can be simultaneously realized.

The oxygen evolution half reaction involves the transport and reaction of four photoinduced holes ($2H_2O + 4\ h^+ \rightarrow O_2 + 4H^+$), which is the crucial process to determine the efficiency of the overall water splitting. Photocatalytic water oxidation usually begins with the reaction of $H_2O^* + h^+ \rightarrow \bullet OH^* + H^+$ (the asterisk indicates the adsorbed state) [170]. Then, •OH* species can be further oxidized to O_2 by a multi-hole migration process [149]. It is established that the vacancy engineering can promote the photocatalytic water oxidation by surmounting the disadvantage of the band structure and facilitating interaction between H_2O molecules and semiconductor surface. Hao et al. synthetized BiOCl nanosheets contained abundant OVs by a solvothermal method [109]. The total yield of oxygen by OV-rich BiOCl reached 1.72 mmol/g after 5 h with silver nitrate as an electron acceptor, which was 3.3 times higher than that by OV-poor BiOCl (0.52 mmol/g) (Fig. 11a). It is worth mentioning that OV-poor and rich BiOCl nanosheets exhibited similar BET surface areas. Under the same experimental conditions, no O_2 evolution was observed in pure BiOCl samples. Because silver nitrate is easy to be reduced under long-time visible light illumination, ferric chloride was also selected as the electron acceptor for oxygen evolution reaction, and the performance is exhibited in Fig. 11b. A similar trend of O_2 evolution can be observed. These results indicate that the enhancement of photooxidation performance can be attributed to the increase of OVs concentration. The existence of OVs not only altered the position of VB and CB, but also induced intermediate energy states within the band gap (Fig. 11c). Besides, the lower position of valence band maximum in OV-rich BiOCl can boost the transfer of holes from the semiconductor to water molecules for oxygen production. Meanwhile, the intermediate band can extend the photo response region up to 648 nm and impede the recombination of photogenerated e^--h^+ pairs. Similarly, Liu et al. demonstrated that IVs can shift down the valence band maximum value of BiOI, which is beneficial to improve the photocatalytic reaction limited by the hole induced half reaction [73]. Furthermore, OVs with certain structure can modulate the water–surface interaction mode toward a better hole trapping for water oxidation [149]. The OVs structures are shown in Fig. 11d, and the OV on the (001) surface causes two nearest Bi atoms around the OV to relax parallel to the (001) surface toward the OV, prolonging the bond length of $Bi_1 - O_1$ (or $Bi_2 - O_2$). Whereas, the OV on the (010) surface leads to an upward relaxation of a neighboring Cl_1 in the direction perpendicular to (010) surface, while the nearest Bi_3 atom relaxes downward (Fig. 11e). The out-of-plane relaxation occurring on the (010) surface shorten the bond length of $Bi_3 - O_1$ (or Bi_3-$- O_2$) from 2.39 to 2.33 Å and the bond length of $Bi_1 - Cl_1$ (or Bi_2-$- Cl_1$) from 2.93 to 2.82 Å. Structure differences of OVs lead to that H_2O on the OVs of (010) surface is more prone to dissociation than on (001) surface, which can be attributed to the following two points. First, the electron transfer from OV on (010) surface to adsorbed water is obviously more favorable than that on (001) surface. Second, the spontaneous dissociation of H_2O adsorbed on the OV of BiOCl-001 can be restricted by steric hindrance, because each bridging O atom is already bound to a proton (Fig. 11d). While on the OV of BOC-010, the Bi site around the OV is suitable for binding the -H fragment dissociated by H_2O. Therefore, compared with the BOC-001 with molecularly adsorbed water on the OVs, BiOCl-010 with dissociatively adsorbed water can promote the first proton removal reaction due to the barrierless O − H bond breaking, leading to much higher photoactivity toward oxidation (Fig. 11f). It is proposed that OVs on the BiOCl surface energize the water oxidation by activating water molecules, while the activation states related to both the electronic structures and geometrical of adsorbed water molecules are highly dependent on the structures of OVs.

5.3. CO_2 reduction

Sustainable photocatalytic CO_2 reduction, which employs inexpensive semiconductor photocatalysts to convert waste CO_2 into

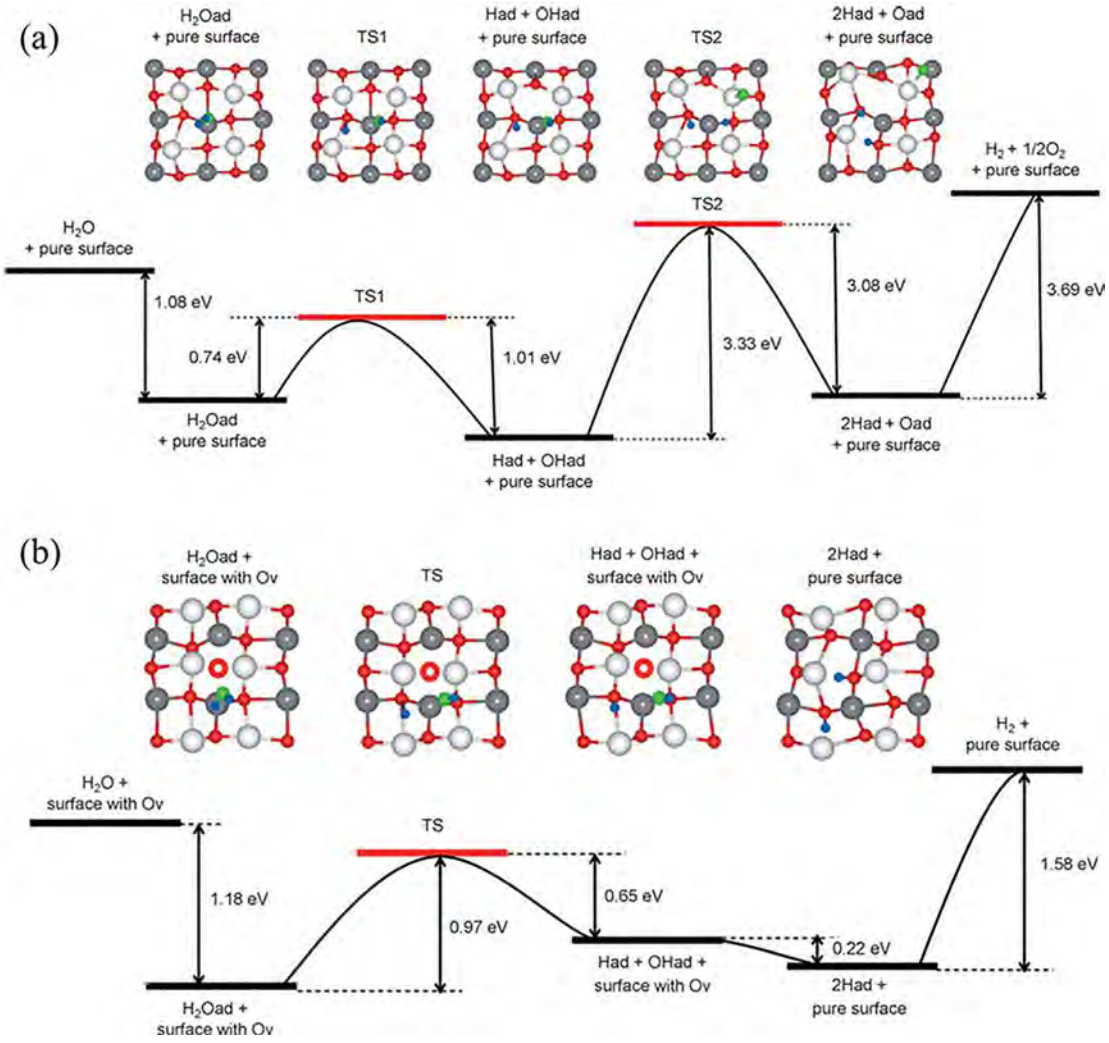

Fig. 10. Overall total-energy profile of the $H_2O = H_2 + 1/2O_2$ reaction on pure BiOCl surface (a) and BiOClsurface with surface OV (b). Surface Bi, subsurface Bi, surface O, H atom of water and O atom of water are in white, grey, red, blue, and green, respectively. Red ring represents surface oxygen vacancy. Reproduced with permission [46]. Copyright 2015, Wiley.

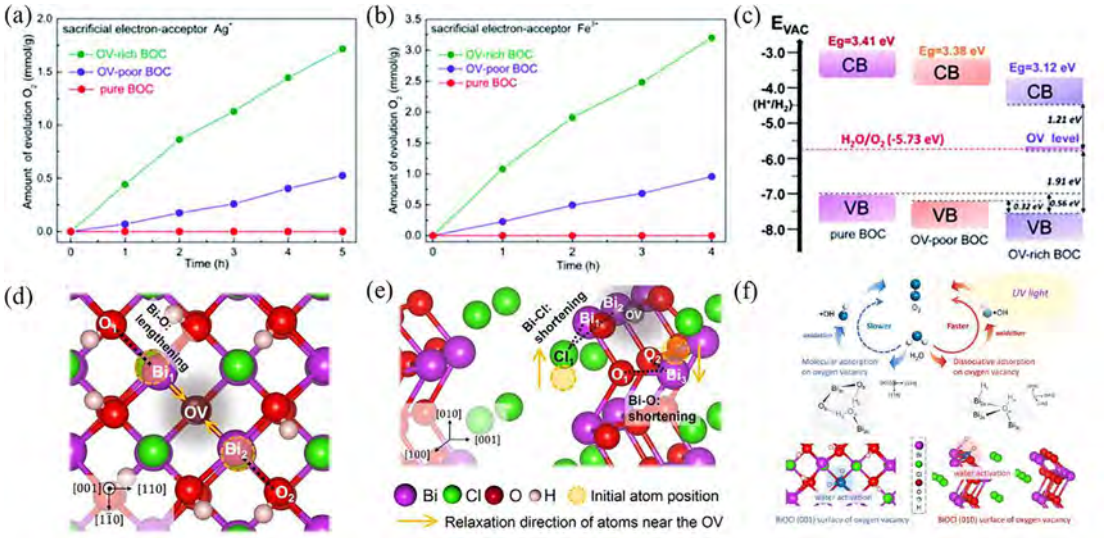

Fig. 11. The production of oxygen from water under visible-light over OV-rich/poor BOC and pure BOC with (a) $AgNO_3$ and (b) $FeCl_3$ as an electron acceptor. (c) the band structure of OV-rich/poor BOC and pure BOC. Reproduced with permission [109]. Copyright 2018, Royal Society of Chemistry. Schematic illustration of the (d) in-plane and (e) out-plane relaxation over the atoms around the OV on the BiOCl (001) and (010) surfaces, respectively. (f) Water oxidation processes mediated by the OVs of BiOCl (001) surface and BiOCl (010) surface. Reproduced with permission [149]. Copyright 2016, American Chemical Society.

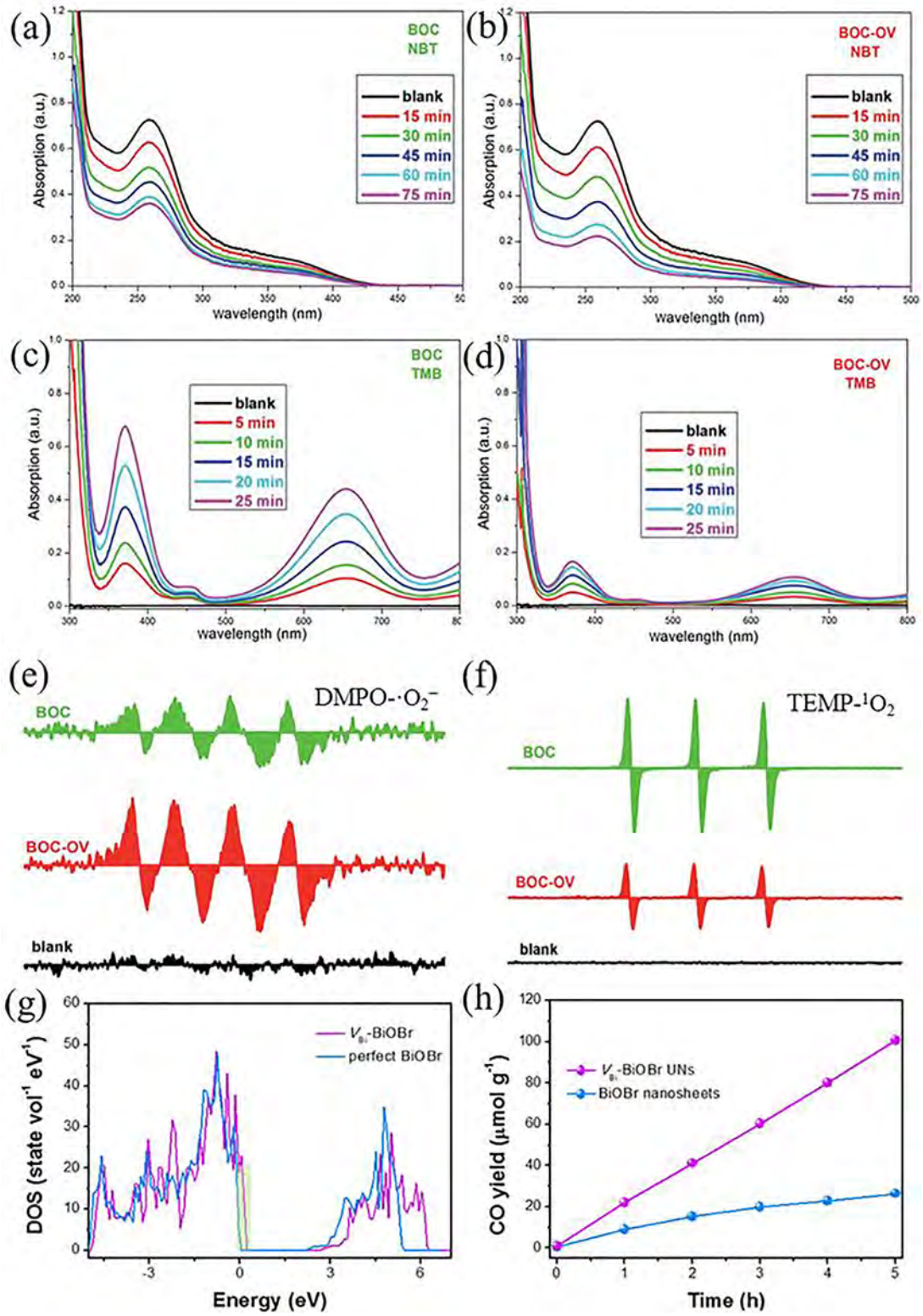

Fig. 12. Time-dependent absorption spectra of NBT oxidation using (a) BiOCl (BOC) and (b) BiOCl-OV (BOC-OV). Time-dependent absorption spectra of TMB oxidation using (c) BOC and (d) BOC-OV. ESR spectra of (e) $\bullet O_2^-$ and (f) $^1O_2$ for BOC-OV and BOC. Reproduced with permission [136]. Copyright 2017, Royal Society of Chemistry. (g) Calculated DOS of perfect BiOBr and V_{Bi}-BiOBr UNs. (h) Photocatalytic CO evolution over and BiOBr nanosheets and V_{Bi}-BiOBr UNs under 300 W Xe lamp irradiation. Reproduced with permission [87]. Copyright 2019, American Chemical Society.

valuable hydrocarbon fuels by taking advantage of solar energy, is an attractive pathway to mitigate greenhouse effect of CO_2 and current energy crisis [171,172]. The hydrocarbon fuels generated in the reduction process include CO, HCHO, HCOOH, CH_3OH, CH_4, C_2H_5OH etc., depending on the number of electrons transferred. However, its reduction efficiency is greatly limited since CO_2 molecule is terrific thermodynamic stable with a high dissociation energy of C═O bond (750 kJ/mol) and a large highest occupied

molecular orbital-lowest unoccupied molecular orbital (HOMO–LUMO) energy gap (13.7 eV) [171]. Recently, vacancy-rich BiOX materials are applied to CO_2 photoreduction because the existence of vacancies facilitates the adsorption of CO_2 and overcome barriers for CO_2 reduction. For the adsorption of CO_2, OVs can act as direct coordinating sites to enhance substrate adsorption and also as charge donor sites to activate CO_2 molecules [149]. Xie et al. induced OVs on the surface of BiOBr atomic layers (OVs-BiOBr ALs) through a 500 W Hg lamp illumination [112]. The existence of OVs enable the OVs-BiOBr ALs to be negatively charged and with fine surface hydrophilicity, which is conducive to CO_2 adsorption on the surface of OVs-BiOBr ALs. DFT results reveal that OVs formation leads to charge delocalization, which can promote the swift transfer of electrons to CO_2 vicinity, and hence effectively reduce it. Moreover, compared with the bulk BiOBr and the BiOBr atomic layers, the OVs-BiOBr ALs can produce more COOH* group, an important intermediate during photoreduction of CO_2 to CO, which indicates that the existence of OVs facilitates the stabilization of the COOH*, and thus to reduce the activation energy of CO_2 and promote the production of CO. By virtue of above advantages, the OVs-BiOBr ALs exhibit unprecedented CO_2 photocatalytic properties with the CO evolution rate of roughly 87.4 mmol/g/h, which is approximately 24 and 20 times higher than that of the bulk BiOBr and the BiOBr atomic layers, respectively.

Ma et al. confirmed that OVs also can induce exciton dissociation for effective photocatalytic CO_2 conversion on flexible BiOCl nanosheets [136]. It is generally agreed that the photocatalytic process consists of excitonic and carrier photocatalytic processes, while only carrier photocatalytic processes are usable for CO_2 reduction reactions. $O_2^{\bullet-}$ and $^1O_2$ are the carriers of photocatalytic process and excitonic photocatalytic process from O_2, respectively. Nitroblue tetrazolium (NBT) and 3,3′,5,5′-tetramethylbenzidine (TMB) can be used to probe $O_2^{\bullet-}$ and $^1O_2$, respectively, for evaluating the functionality of OVs on the photocatalytic process. The UV–Vis absorption spectra (Fig. 12a and b) were employed to evaluate the NBT oxidation, which reveals that the existence of OVs favors the generation of $O_2^{\bullet-}$ [136]. Fig. 12c and d displays that BiOCl with stronger TMB oxidation UV–Vis absorption spectra than BiOCl-OV, which indicates that the generation of $^1O_2$ is suppressed by OVs. Electron spin resonance (ESR) (Fig. 12e-f) also confirms that BiOCl-OV with an enhancing amount of $O_2^{\bullet-}$ and a decreasing amount of $^1O_2$ compared with BiOCl. These results indicate that OVs can simultaneously induce exciton dissociation and promote the carrier photocatalytic process. Therefore, under UV–Vis light, BiOCl-OV exhibits higher reduction efficiency for CO_2 compared with BiOCl.

Apart from OVs, cation vacancies are also beneficial for the CO_2 reduction activity improvement by a similar working manner. For example, Liu et al. synthesized ultrathin BiOBr nanosheets with abundant surface BiVs (V_{Bi}-BiOBr UNs) [87]. The presence of BiVs tunes the electronic structure of BiOBr, which leads to UV − vis diffuse reflection spectra red shift of V_{Bi}-BiOBr UNs. Simultaneously, the DFT calculation indicates that density of states (DOS) at the VB edge of V_{Bi}-BiOBr is higher than that of pristine BiOBr (Fig. 12g). It means that the charge density around the Fermi level is increased by engineered BiVs, suggesting that more charge carriers can participate in the photoreduction of CO_2. Furthermore, the CO_2 adsorption isotherms shows that V_{Bi}-BiOBr UNs with larger adsorption capacity can ensure more CO_2 to involve in the interfacial reduction process. The in situ FTIR spectroscopy over V_{Bi}-BiOBr UNs demonstrates that the presence of BiVs helps to activate CO_2 into COOH* group. Therefore, V_{Bi}-BiOBr UNs exhibits excellent CO evolution rate of approximately 20.1 μmol/g/h with a 98% selectivity, which is about 3.8 times higher than that of the pristine BiOBr nanosheets (Fig. 12h).

5.4. Nitrogen fixation

Compared with water splitting and CO_2 reduction, the nitrogen fixation is more

challenging due to the weak adsorption of N_2 molecules on the semiconductor surface, the high dissociation energy of stubborn triple bond of N_2 (962 kJ mol^{-1}), the high-energy N_2 intermediates in the reduced or protonated form (N_2^- or N_2H), and the multielec-

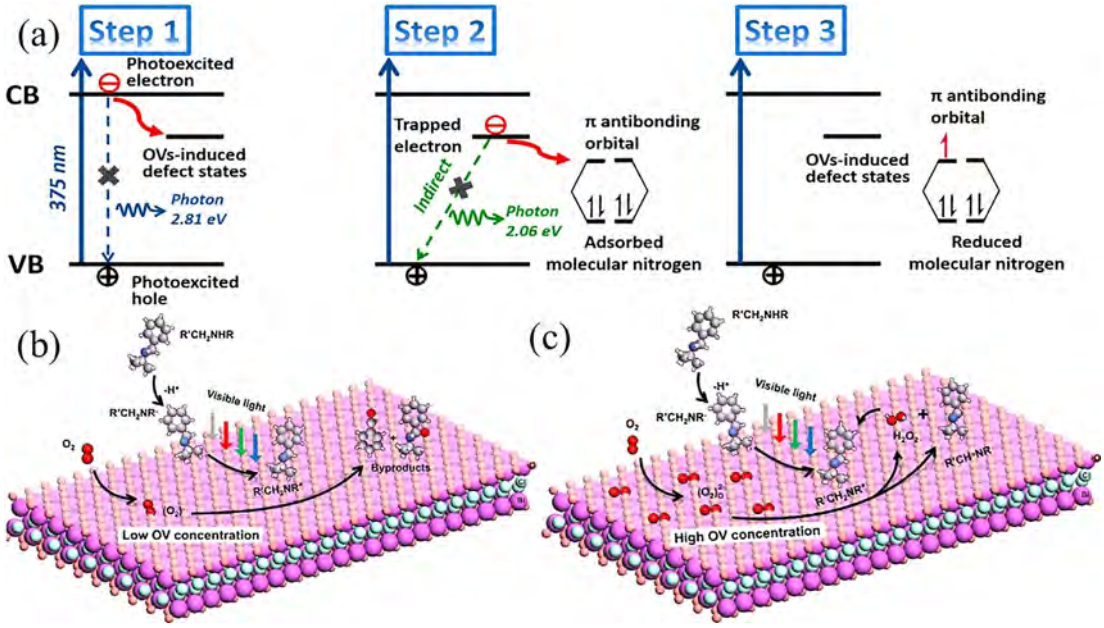

Fig. 13. (a) Schematic illustration for improved interfacial electron transfer processes induced by OVs. OVs-induced intermediate states first dynamically capture the directly photoexcited electrons from the CB, thus inhibiting the direct recombination of charge carriers (Step 1 and 2). Subsequently, the indirect recombination of captured electrons with photogenerated holes is also suppressed as the captured electrons could efficiently be transferred to populate the empty antibonding orbitals of adsorbed N_2 (Step 3). Reproduced with permission [45]. pubs.acs.org/doi/10.1021/jacs.5b03105 Copyright 2015, American Chemical Society. Reaction scheme for the aerobic oxidation of BA to BI on BiOCl {001} facets with low (b) or high (c) OV concentration. R = t-Bu, R' = Ph. Reproduced with permission [111]. Copyright 2018, Elsevier.

tron nature of the reaction [43,89,173,174]. Fortunately, OVs with abundant localized electrons can facilitate the adsorption and activation of N_2 molecules [45]. OVs can adsorb N_2 with an end-on configuration by coordinating with the two OV-connected and partially reduced Bi atoms [45]. Then, the OVs promote the electrons transfer from the excited BiOBr to the π antibonding orbitals of N_2, thus to achieve efficient photoreduction from N_2 to ammonia (Fig. 13a) [45]. The photocatalytic fixation rate of this OVs mediated BiOBr reached 104.2 $\mu mol \cdot h^{-1} \cdot g^{-1}$ without using any precious-metal cocatalysts or organic scavengers, while the ammonia produced by the perfect BiOBr counterpart was negligible [45]. In the OVs mediated BiOI (R-BiOI), Bai et al. proposed that the presence of OVs can induce the generation of unsaturated metal ions and the form of chemical environment with abundant Lewis-base on the surface of BiOI, and thus facilitate the N_2 adsorption and favor the transportation of electrons to adsorbed N_2 molecules [65]. Therefore, under a small external bias (0.4 V vs RHE), the obvious production of ammonia (1.4 $mmol \cdot m^{-2} \cdot h^{-1}$) can be accomplished in photoelectrochemical system with R-BiOI as photocathode. Furthermore, Li et al. clarified that OVs can also improve the kinetic feasibility of N_2 fixation because of its indispensable roles on providing lower molecular steps amendable for the N–N triple bond cleavage via the electron transfer assisted by protons [175].

The structure of OVs, which can influence both the adsorption structure and the activation level of N_2, strongly determine the selectivity of N_2 fixation [45,175]. OVs on the different BiOCl surfaces interacts differently with N_2 leading to distinct N_2 fixation pathways [175]. On the OVs of BiOCl (001) surface, N_2 bonded with an end-on configuration possesses a larger steric hindrance at vicinal nitrogen atom and low coordination number at the terminal nitrogen atom. This configuration determines that hydrogenation of the adsorbed N_2 moiety prefers to begin with the terminal nitrogen atom rather than the coordinated one. Thus, the fixation of N_2 is achieved by continuous hydrogenation of the most distant nitrogen atom, the NH_3 is finally liberated with cleaved N–N triple bond, which is regarded as the distal mechanism in an asymmetric fashion. Whereas, as for side-on bridging N_2 on the OVs of BiOCl (010) surface with two equally charged nitrogen atoms, N_2 reduction to NH_3 often follows an alternative mechanism with a symmetric pathway via alternative hydrogenating on the N atoms to produce N_2H_2-level and N_2H_4-level intermediates. Similarly, with the assistance of OVs, BiOBr with OVs on the exposed (001) facets and Bi2MoO6/OV-BiOBr heterojunctions both possessed excellent selectivity in the process of photocatalytic N_2 fixation to NH_3, with tiny byproducts such as N_2H_4, NO^{2-} and NO^{3-} [45,176].

5.5. Selective photocatalytic oxidation

As mentioned above, vacancy regulation can adjust the types of ROS produced, which further turns the selective photocatalytic oxidation into reality. The generation of $\cdot O_2^-$ with strong oxidation ability will lead to overoxidation and produce overoxidized products, while participation of $^1O_2$ can avoid this situation, so as to realize selective oxidation. Chen et al. carried out photocatalytic oxidation experiments of thioether and triphenylphosphine using BiOBr samples [147]. In the presence of large $V_{Br}^{\bullet}V_O^{\bullet\bullet}V_{Bi}'''$ triple atom vacancy cluster, $^1O_2$ is the main active substance in the process of photocatalysis, and nearly 93% of thioanisole is converted to the corresponding sulfoxide (99%, selectivity), which indicates that this reaction possesses a high yield and selectivity. For comparison, in the presence of V_{Bi}''' $V_O^{\bullet\bullet}$, although the conversion of the reaction reaches 84%, the yield of target product (sulfoxide) is very small. There are many overoxidized products, such as methylsulfonylbenzene, indicating the poor selectivity of it. Zhang et al. tuned the structure of OVs on the (001) facets of BiOCl by adjusting OVs concentration, thus realizing the photocatalytic selective oxidation of butylbenzylamine (BA) to N-*tert*-butylbenzylimine (BI) [111]. They prepared the BiOCl with OVs (BOC-OV-3) by a hot ethylene glycol mediated solvothermal method. Then they applied H_2O_2 coupled infrared irradiation to obtain BOC-OV-2 and BOC-OV-1 with less vacancies. BOC-OV-0 was obtained by fully oxidizing the surface of OV-1 via annealing under O_2 atmosphere. The smaller value of X in BOC-OV-X means the lower concentration of OVs, and 0 means there is no OVs on the BiOCl surface. The overall BA conversions by BOC-OV-3, BOC-OV-2, BOC-OV-1, and BOC-OV-0 are 85%, 72%, 59%, and 4%, with corresponding BI selectivity of 87%, 75%,62%, and 0, respectively. The improved BA conversion by BOC-OV-3, BOC-OV-2 and BOC-OV-1 can be ascribed to the enhanced visible light absorbance resulting from higher OVs concentration. The associated high BI selectivity should be explored from the oxidants. In this study, both photogenerated h^+ and ROS ($\cdot O_2^-$ and O_2^{2-}) participated in the photocatalytic selective oxidation BA. BOC-OV-X samples almost share the same VB positions, and both the reactant and the product can be oxidized by their photoexcited h^+, so the traditional VB position dominated selective oxidation cannot explain the high selectivity. Subsequently, ROS trapping experiments displayed that the addition of superoxide dismutase (SOD, which catalyzes the disproportionation of $\cdot O_2^-$ into H_2O_2 and O_2) enhanced the BI selectivity from 87% to 99% for BOC-OV-3, from 75% to 98% for BOC-OV-2, and from 62% to 79% for BOC-OV-1, respectively. These results figure out that $\cdot O_2^-$ leads to the over oxidization, and H_2O_2 (O_2^{2-}) is the reason for the high BI selectivity. BiOCl (001) surface with low concentration OVs prefers to activate O_2 to produce $\cdot O_2^-$ via a one-electron reduction process (Fig. 13b), but the counterpart with high concentration OVs favors the generation of O_2^{2-} through a two-electron reduction process (Fig. 13c), because more electrons are less localized and Bi-O and Bi-Bi bond lengths are shortened on the BiOCl (001) surface with high OVs concentration. Therefore, OV-3 samples possess the high selectivity in the process of photocatalytic selective oxidation BA. This result is consistent with the above conclusion that the structure of OVs can affect the molecular oxygen activation state. Therefore, the regulation of surface molecular processes by intelligent vacancy engineering is considered as the hinge of selective photocatalytic oxidation.

5.6. Other potential applications

The existence of vacancies not only improves the performance of BiOX in the above-mentioned common applications, but also makes BiOX have better performance in some unique fields. For instance, abundant OVs on BiOCl helped to improve the sensitivity of the photocathodic immunosensor [177]. The OVs can promote the complete reduction of electron acceptors (i.e·H_2O_2 and O_2), thus amplifying the detection signal to achieve strong sensitivity. Wu et al. established that OVs formed on the BiOBr (001) facets strongly affect their band structures leading to better photooxidation and higher mobility of h^+ [116]. Simultaneously, OVs promoted the activation of molecular oxygen to produce more $\bullet O_2^-$. The resulting effective accumulation of h^+ and $\bullet O_2^-$ ultimately leads to the excellent photocatalytic *E. coli K-12* inactivation performance over BiOBr with fully exposed (001) facets. Interestingly, a reversible photocatalytic color switching system was fabricated by mixing the oxygen deficient-BiOCl nanosheets with redox dyes [178]. In this system, OVs act as sacrificial electron donors to scavenge photoexcited holes and thus endow BiOCl excellent photoreductive activity under UV irradiation. Therefore, under UV light illumination, BiOCl nanosheet with abundant OVs can reduce the dye and make it fade, while the color can switch back reversibly by oxygen oxidation in air. Integrating this system with poly(vinyl

alcohol) hydrogel to form a transparent and flexible gel film still possesses excellent photoconversion effect which can be applied as a colorimetric oxygen indicator for monitoring oxygen leakage. Furthermore, Guan et al. synthesized OVs-rich BiOBr/ $Ru(bpy)_2CpyCl_2$ (BiOBr–H/Rub_2d) for photodynamic therapy [179]. The existence of OVs promoted the generation singlet oxygen in tumor cells under light illumination, leading to strong ablation effects both *in vitro* and *in vivo*. Therefore, vacancy engineering shows great potential in the development of effective theranostic agents for cancer therapy.

6. Summary and future perspectives

In summary, this review article highlights an overview of recent studies related to the vacancy engineered BiOX for solar energy conversion. We gather the fundamental understanding on the functionality of vacancies in improving the BiOX photocatalytic performance, and summarize the rational vacancy design of BiOX for manipulating photocatalytic transformation pathway. The existence of vacancies in BiOX not only can alter the semiconductor intrinsic properties of BiOX to extend light harvesting, boost exciton dissociation, and manipulate charge transfer and separation, but also play a significant part in promoting the redox reaction on the semiconductor surface by furnishing active sites for adsorption, dissociation, and activation of substrates. The types, structures, and concentrations of vacancies in BiOX can appreciably affect the function of vacancies, which can be determined by advanced characterization techniques, including computational characterization. Vacancy engineering has greatly improved the photocatalytic performance of BiOX in pollutant removal, water splitting, CO_2 reduction, nitrogen fixation, and so on (Table 2), and also made them be applicated in some interesting fields (such as selective organic conversion), laying the foundation for expanding the application of BiOX.

Although some encouraging results have been obtained, the research of vacancy engineering for ameliorating BiOX photocatalytic performance is still in an early stage and thereby leaves much room for further evolution. Firstly, although there are many methods to introduce vacancies into BiOX, it is still difficult to precisely map the concentration and distribution of vacancies. Simultaneously, the relationship between the concentration and distribution of vacancies on the intrinsic properties of BiOX is rarely reported. In addition, the formation of vacancy is not always beneficial to the photocatalytic performance of BiOX. For example, the vacancy can become the recombination center of the e^--h^+ pairs, thus reducing the carrier density. Therefore, in order to avoid the adverse effects of vacancies, future research should not only actively explore sophisticated methods for vacancy introduction, but also make full use of advanced characterization technology and systematic DFT studies to guide vacancy engineering and clarify their influence on properties.

Secondly, in order to adapt to the more refined vacancy design, the characterization method also needs corresponding progress. For example, we need to accurately quantify the vacancy content, rather than limited the measurement to semiquantitative ways. Simultaneously, in situ characterization and clearer visualization should also be developed to explore the changes and roles of vacancies during the photocatalytic reaction process.

Thirdly, BiOX with vacancy-rich architecture always suffer from relatively low physicochemical stability. Especially the OVs-rich BiOX, which can be repaired by ambient O_2 or H_2O during the long-term photocatalytic process. Thus, it is necessary to expand the research on Bi vacancy, halogen vacancy, multi-vacancy or vacancy associates, and explore methods to stabilize the dominant vacancies structure in BiOX. Furthermore, the solutions of the stability issue may be explored from the following aspects. (1) Core-shell structure preparation with less-stable BiOX as the core is probably effective design strategies to mitigate the BiOX related stability problems. (2) Construction of subsurface vacancies. The unsaturated bonding and exposed nature of surface vacancies often leads to poor stability during photocatalysis functioning. However, subsurface vacancies below regions of the vacancies-free surface possess substantially extended lifetime due to their insensitivity to oxygen species produce during the reaction. Besides, subsurface vacancies can steadily promote the chemical activity of the near-surface region. Given the promising performance of subsurface vacancies, more novel and effective approaches should be developed to control the creation of subsurface vacancies. (3) Introduce new active center for adsorbing and activating substrate and/or oxygen species and thus preventing the adverse occupation of vacancies. For example, it is reported that Bi metal nanoparticles can serve as the active site to active H_2O and O_2 so that the OVs will not be restored by O_2 and H_2O molecules, thereby preventing the deactivation of OVs [180]. (4) Introduction of visible light-switchable oxygen vacancies. The introduction of visible light-switchable OVs in BiOX can be achieved by constructing unstable surfaces through morphology control. The weak Bi-O bonding on the unstable surface contributes to the easy escape of O atoms, thus the visible light irradiation in the photocatalytic reaction is enough for the generation of OVs. when the light is turned off, the OVs can be refilled by seizing the surrounding O atoms to restore BiOX to the original OVs-free composition, leading to a sustainable and reversible generation of OVs by light control. Therefore, BiOX with visible light-switchable OVs is likely to have stable and efficient photocatalytic performance under mild conditions.

Fourthly, the study of structure–activity relationship of vacancy is inadequate. It has been acknowledged that the structure of vacancies can affect the adsorption mode of oxygen molecules, resulting in different activated species, thus modulating the photocatalytic pathways. Besides, the vacancy structure is widely considered to be determined by the element composition of the BiOX crystal facets, while some researchers believe that the vacancy concentration also matters. Therefore, more methods should be explored to control the vacancy structure. In this way, vacancies with special functions will not to be limited to a single crystal facet, but can be introduced into the dominant crystal plane, so as to give full play to the advantages of the dominant crystal plane and vacancies. In addition, further endeavor is desired to clearly clarified the authentic correlation between the vacancy structure, adsorption mode of molecular oxygen and the activated state of oxygen molecule.

Fifthly, vacancies can serve as active sites to directly participate in the photocatalytic reactions by building strong interaction with substrate, but the existing researches lack the discussion on the competitive reactions on vacancies, which may limit the further improvement of photocatalytic efficiency. Therefore, it is important to suppress the competitive reactions that may occur in the vicinity of vacancies. In order to better achieve the desired purpose, the following aspects can be considered to control the competition reactions. (1) It is reported that vacancies can regulate the position of VBM and CBM, which is directly related to the redox capability of the photocatalyst, therefore it is important to prepare BiOX with suitable band structure according to the purpose. For example, with the purpose of CO_2 reduction, it is better to move the CBM and VBM upward, thus enhancing the reducibility of electrons while reducing the oxidation of holes, which can inhibit the occurrence of reverse oxidation reactions. (2) Given that the structure of OVs can affect the pathway of photocatalytic reaction, it is reasonable to control the direction of photocatalytic reaction by adjusting the structure of OVs. (3) The synergistic effect of vacan-

cies and functional groups is also expected to inhibit the occurrence of competitive reactions. For example, functionalized amine shows excellent affinity with molecules of CO_2, which can improve the adsorption capacity of CO_2, thereby promoting the CO_2 reaction directionally [181,182].

Sixthly, in the past decades, BiOX with open layered crystalline structure exhibited excellent performance in photocatalytic degradation, while their application in CO_2 photoreduction and nitrogen fixation was far from satisfactory. Fortunately, vacancy engineering makes BiOX stand out in the field of CO_2 photoreduction and nitrogen fixation. Besides, with the assistance of vacancy engineering, the applications of BiOX in selective photocatalysis, photocathodic immunosensor, photocatalytic bacteriostasis, photodynamic therapy, and so on have gradually attracted attention [116,177,179]. However, these applications are still in infant moment and far away from practical applications. Vacancy engineering should be better combined with heterostructure construction, photosensitization, crystal face control, and other approaches to strive for further improvement. In particular, the immobilization technology of BiOX should also be paid great attention to promote the practical application.

Declaration of Competing Interest

The authors declare that they have no known competing financial interests or personal relationships that could have appeared to influence the work reported in this paper.

Acknowledgments

This work was supported by the Natural Science Foundation of Hunan Province (2019JJ20002), the Foundation for Innovative Research Groups of the National Natural Science Foundation of China (51979101, 51679082, 51521006, 51809184), the Hunan Science & Technology Innovation Program (2018RS3037).

References

[1] Y. Qian, D. Li, Y. Han, H.L. Jiang, J. Am. Chem. Soc. 142 (2020) 20763–20771.
[2] L. Jiang, X. Yuan, G. Zeng, Z. Wu, J. Liang, X. Chen, L. Leng, H. Wang, H. Wang, Appl. Catal., B 221 (2018) 715–725.
[3] N. Tang, J. Liang, C. Niu, H. Wang, Y. Luo, W. Xing, S. Ye, C. Liang, H. Guo, J. Guo, Y. Zhang, G. Zeng, J. Mater. Chem. A 8 (2020) 7588–7625.
[4] W. Xing, J. Liang, W. Tang, D. He, M. Yan, X. Wang, Y. Luo, N. Tang, M. Huang, Desalination 482 (2020).
[5] K.H.A. Fujishima, Nature 238 (1972) 37–38.
[6] J. Zhang, X. Yuan, M. Si, L. Jiang, H. Yu, Adv. Colloid Interface Sci. 282 (2020) 102209.
[7] H. Wang, Y. Sun, Y. Wu, W. Tu, S. Wu, X. Yuan, G. Zeng, Z.J. Xu, S. Li, J.W. Chew, Appl. Catal., B 245 (2019) 290–301.
[8] K. Afroz, M. Moniruddin, N. Bakranov, S. Kudaibergenov, N. Nuraje, J. Mater. Chem. A 6 (2018) 21696–21718.
[9] G. Zhang, Z.A. Lan, X. Wang, Chem. Sci. 8 (2017) 5261–5274.
[10] S. Cao, T.-S. Chan, Y.-R. Lu, X. Shi, B. Fu, Z. Wu, H. Li, K. Liu, S. Alzuabi, P. Cheng, M. Liu, T. Li, X. Chen, L. Piao, Nano Energy 67 (2020).
[11] X. Chen, R. Shi, Q. Chen, Z. Zhang, W. Jiang, Y. Zhu, T. Zhang, Nano Energy 59 (2019) 644–650.
[12] H. Sun, P. Qin, Z. Wu, C. Liao, J. Guo, S. Luo, Y. Chai, J. Alloys Compd. 834 (2020).
[13] J. Guo, L. Jiang, J. Liang, W. Xu, H. Yu, J. Zhang, S. Ye, W. Xing, X. Yuan, Chemosphere (2020) 128651.
[14] Y. Wu, H. Wang, W. Tu, Y. Liu, S. Wu, Y.Z. Tan, J.W. Chew, Appl. Catal., B 233 (2018) 58–69.
[15] W. Wang, Q. Niu, G. Zeng, C. Zhang, D. Huang, B. Shao, C. Zhou, Y. Yang, Y. Liu, H. Guo, W. Xiong, L. Lei, S. Liu, H. Yi, S. Chen, X. Tang, Appl. Catal., B (2020) 273.
[16] Y. Pan, X. Yuan, L. Jiang, H. Wang, H. Yu, J. Zhang, Chem. Eng. J. 384 (2020).
[17] M. Gao, J. Yang, T. Sun, Z. Zhang, D. Zhang, H. Huang, H. Lin, Y. Fang, X. Wang, Appl. Catal., B 243 (2019) 734–740.
[18] C. Bie, B. Zhu, F. Xu, L. Zhang, J. Yu, Adv. Mater. 31 (2019) e1902868.
[19] M. Wang, J. Liu, C. Guo, X. Gao, C. Gong, Y. Wang, B. Liu, X. Li, G.G. Gurzadyan, L. Sun, J. Mater. Chem. A 6 (2018) 4768–4775.
[20] N. Zhang, L. Li, Q. Shao, T. Zhu, X. Huang, X. Xiao, A.C.S. Appl, Energy Mater. 2 (2019) 8394–8398.
[21] F. Xu, J. Zhang, B. Zhu, J. Yu, J. Xu, Appl. Catal., B 230 (2018) 194–202.
[22] P. Qiu, C. Xu, N. Zhou, H. Chen, F. Jiang, Appl. Catal., B 221 (2018) 27–35.
[23] R. Guan, D. Wang, Y. Zhang, C. Liu, W. Xu, J. Wang, Z. Zhao, M. Feng, Q. Shang, Z. Sun, Appl. Catal., B (2021) 282.
[24] L. Marzo, S.K. Pagire, O. Reiser, B. Konig, Angew. Chem., Int. Ed. Engl. 57 (2018) 10034–10072.
[25] D. Friedmann, A. Hakki, H. Kim, W. Choi, D. Bahnemann, Green Chem. 18 (2016) 5391–5411.
[26] L. Jiang, X. Yuan, G. Zeng, J. Liang, X. Chen, H. Yu, H. Wang, Z. Wu, J. Zhang, T. Xiong, Appl. Catal., B 227 (2018) 376–385.
[27] H. Yu, L. Jiang, H. Wang, B. Huang, X. Yuan, J. Huang, J. Zhang, G. Zeng, Small 15 (2019) e1901008.
[28] J. Guo, J. Liang, X. Yuan, L. Jiang, G. Zeng, H. Yu, J. Zhang, Chem. Eng. J. 352 (2018) 782–802.
[29] X. Chen, X. Peng, L. Jiang, X. Yuan, H. Yu, H. Wang, J. Zhang, Q. Xia, Chem. Eng. J. 395 (2020).
[30] J. Zhang, H. Wang, X. Yuan, G. Zeng, W. Tu, S. Wang, J. Photochem. Photobiol., C 38 (2019) 1–26.
[31] Q. Xiang, J. Yu, M. Jaroniec, Chem. Soc. Rev. 41 (2012) 782–796.
[32] J. Li, Y. Yu, L. Zhang, Nanoscale 6 (2014) 8473–8488.
[33] L. Ye, Y. Su, X. Jin, H. Xie, C. Zhang, Environ. Sci.: Nano 1 (2014) 90.
[34] H. Yu, B. Huang, H. Wang, X. Yuan, L. Jiang, Z. Wu, J. Zhang, G. Zeng, J. Colloid Interface Sci. 522 (2018) 82–94.
[35] Y. Guo, W. Shi, Y. Zhu, Y. Xu, F. Cui, Appl. Catal., B (2020) 262.
[36] T. Li, C. Wang, T. Wang, L. Zhu, Appl. Catal., B, 268 (2020).
[37] S. Cui, G. Shan, L. Zhu, Appl. Catal., B 219 (2017) 249–258.
[38] H. Yu, J. Huang, L. Jiang, X. Yuan, K. Yi, W. Zhang, J. Zhang, H. Chen, Chem. Eng. J. (2020).
[39] K. Zhang, C. Liu, F. Huang, C. Zheng, W. Wang, Appl. Catal., B 68 (2006) 125–129.
[40] H. Zhao, X. Liu, Y. Dong, Y. Xia, H. Wang, Appl. Catal., B (2019) 256.
[41] L. Jing, W. Zhou, G. Tian, H. Fu, Chem. Soc. Rev. 42 (2013) 9509–9549.
[42] L. Zhang, W. Wang, D. Jiang, E. Gao, S. Sun, Nano Res. 8 (2014) 821–831.
[43] J. Li, H. Li, G. Zhan, L. Zhang, Acc. Chem. Res. 50 (2017) 112–121.
[44] M. Guan, C. Xiao, J. Zhang, S. Fan, R. An, Q. Cheng, J. Xie, M. Zhou, B. Ye, Y. Xie, J. Am. Chem. Soc. 135 (2013) 10411–10417.
[45] H. Li, J. Shang, Z. Ai, L. Zhang, J. Am. Chem. Soc. 137 (2015) 6393–6399.
[46] L. Zhang, Z. Han, W. Wang, X. Li, Y. Su, D. Jiang, X. Lei, S. Sun, Chemistry 21 (2015) 18089–18094.
[47] X. Tong, X. Cao, T. Han, W.-C. Cheong, R. Lin, Z. Chen, D. Wang, C. Chen, Q. Peng, Y. Li, Nano Res. 12 (2019) 1625–1630.
[48] L. Ye, Y. Su, X. Jin, H. Xie, C. Zhang, Environ. Sci.: Nano 1 (2014).
[49] X. Jin, L. Ye, H. Xie, G. Chen, Coord. Chem. Rev. 349 (2017) 84–101.
[50] H. Li, J. Li, Z. Ai, F. Jia, L. Zhang, Angew. Chem., Int. Ed. Engl. 57 (2018) 122–138.
[51] Y. Liu, C. Xiao, Z. Li, Y. Xie, Adv. Energy Mater. 6 (2016).
[52] G. Li, G.R. Blake, T.T. Palstra, Chem. Soc. Rev. 46 (2017) 1693–1706.
[53] X. Zhang, L. Zhao, C. Fan, Z. Liang, P. Han, Comput. Mater. Sci. 61 (2012) 180–184.
[54] Y. Huang, H. Li, M.-S. Balogun, W. Liu, Y. Tong, X. Lu, H. Ji, A.C.S. Appl, Mater. Interfaces 6 (2014) 22920–22927.
[55] L. Ye, K. Deng, F. Xu, L. Tian, T. Peng, L. Zan, Phys. Chem. Chem. Phys. 14 (2012) 82–85.
[56] L. Ye, L. Zan, L. Tian, T. Peng, J. Zhang, Chem. Commun. (Cambridge, U. K.) 47 (2011) 6951–6953.
[57] H. Li, J. Shi, K. Zhao, L. Zhang, Nanoscale 6 (2014) 14168–14173.
[58] S. Wu, J. Xiong, J. Sun, Z.D. Hood, W. Zeng, Z. Yang, L. Gu, X. Zhang, S.-Z. Yang, ACS Appl. Mater. Interfaces 9 (2017) 16620–16626.
[59] J. Gan, B.B. Rajeeva, Z. Wu, D. Penley, Y. Zheng, Electrochim. Acta 219 (2016) 20–27.
[60] C. Hua, X. Dong, Y. Wang, N. Zheng, H. Ma, X. Zhang, J. Mater. Sci. 54 (2019) 9397–9413.
[61] Y. Lv, Y. Liu, Y. Zhu, Y. Zhu, J. Mater. Chem. A 2 (2014) 1174–1182.
[62] Q. Li, S. Gao, J. Hu, H. Wang, Z. Wu, Catal. Sci. Technol. 8 (2018) 5270–5279.
[63] M. Sun, W. Zhang, Y. Sun, Y. Zhang, F. Dong, Chin. J. Catal. 40 (2019) 826–836.
[64] J. Hu, G. Xu, J. Wang, J. Lv, X. Zhang, Z. Zheng, T. Xie, Y. Wu, New J. Chem. 38 (2014) 4913–4921.
[65] Y. Bai, H. Bai, K. Qu, F. Wang, P. Guan, D. Xu, W. Fan, W. Shi, Chem. Eng. J. 362 (2019) 349–356.
[66] L. Zhang, Z. Wang, C. Hu, B. Shi, Appl. Catal., B, 257 (2019).
[67] H. Wang, D. Yong, S. Chen, S. Jiang, X. Zhang, W. Shao, Q. Zhang, W. Yan, B. Pan, Y. Xie, J. Am. Chem. Soc. 140 (2018) 1760–1766.
[68] Y. Li, T. Liu, Z. Cheng, Y. Peng, S. Yang, Y. Zhang, Chem. Eng. J. (2020).
[69] Z.K. Cui, L.W. Mi, Z. Zheng, G.H. Wang, W.J. Fa, Adv. Mater. Res. 726–731 (2013) 646–649.
[70] D. Kim, D. Jung, Chem. Phys. Lett. 674 (2017) 130–135.
[71] Y. Yang, Z. Zeng, C. Zhang, D. Huang, G. Zeng, R. Xiao, C. Lai, C. Zhou, H. Guo, W. Xue, M. Cheng, W. Wang, J. Wang, Chem. Eng. J. 349 (2018) 808–821.
[72] Y. Guan, J. Wu, X. Man, Q. Liu, Y. Qi, P. He, X. Qi, Chem. Eng. J. 396 (2020).
[73] X. Wang, C. Zhou, L. Yin, R. Zhang, G. Liu, ACS Sustainable Chem. Eng. 7 (2019) 7900–7907.
[74] H. Xia, Q. Wang, Chem. Mater. 14 (2002) 2158–2165.
[75] P.A. Osorio-Vargas, C. Pulgarin, A. Sienkiewicz, L.R. Pizzio, M.N. Blanco, R.A. Torres-Palma, C. Pétrier, J.A. Rengifo-Herrera, Ultrason. Sonochem. 19 (2012) 383–386.

[76] W. Fan, H. Li, F. Zhao, X. Xiao, Y. Huang, H. Ji, Y. Tong, Chem. Commun. (Cambridge, U. K.) 52 (2016) 5316–5319.
[77] D. Wu, X. Wang, H. Wang, F. Wang, D. Wang, Z. Gao, X. Wang, F. Xu, K. Jiang, J. Colloid Interface Sci. 533 (2019) 539–547.
[78] J. Jiang, L. Zhang, H. Li, W. He, J.J. Yin, Nanoscale 5 (2013) 10573–10581.
[79] Y. Shiraishi, M. Hashimoto, K. Chishiro, K. Moriyama, S. Tanaka, T. Hirai, J. Am. Chem. Soc. 142 (2020) 7574–7583.
[80] L. Ye, X. Jin, Y. Leng, Y. Su, H. Xie, C. Liu, J. Power Sources 293 (2015) 409–415.
[81] H. Xing, H. Ma, Y. Fu, X. Zhang, X. Dong, X. Zhang, J. Renewable Sustainable Energy 7 (2015).
[82] H. Yu, J. Huang, L. Jiang, Y. Shi, K. Yi, W. Zhang, J. Zhang, H. Chen, X. Yuan, Chem. Eng. J. 402 (2020).
[83] Y. Sun, G. Li, W. Wang, W. Gu, P.K. Wong, T. An, J. Environ. Sci. 84 (2019) 69–79.
[84] X. Wang, Q. Li, C. Zhou, R. Zhang, Appl. Surf. Sci. 493 (2019) 657–664.
[85] J. Xu, Y. Teng, F. Teng, Sci. Rep. 6 (2016) 32457.
[86] Y. Teng, F. Teng, Electrochim. Acta 244 (2017) 1–7.
[87] J. Di, C. Chen, C. Zhu, P. Song, J. Xiong, M. Ji, J. Zhou, Q. Fu, M. Xu, W. Hao, J. Xia, S. Li, H. Li, Z. Liu, A.C.S. Appl, Mater. Interfaces 11 (2019) 30786–30792.
[88] J. Sun, D. Li, Y. Cai, Z. Zou, H. Zhang, J. Gong, L. Sun, H. Xu, D. Xia, J. Mater. Sci.: Mater. Electron. 29 (2018) 12241–12250.
[89] X. Xue, R. Chen, H. Chen, Y. Hu, Q. Ding, Z. Liu, L. Ma, G. Zhu, W. Zhang, Q. Yu, J. Liu, J. Ma, Z. Jin, Nano Lett. 18 (2018) 7372–7377.
[90] J. Di, C. Zhu, M. Ji, M. Duan, R. Long, C. Yan, K. Gu, J. Xiong, Y. She, J. Xia, H. Li, Z. Liu, Angew. Chem., Int. Ed. Engl. 57 (2018) 14847–14851.
[91] J. Lin, Z. Hu, H. Li, J. Qu, M. Zhang, W. Liang, S. Hu, Inorg. Chem. 58 (2019) 9833–9843.
[92] M. Ji, J. Di, Y. Liu, R. Chen, K. Li, Z. Chen, J. Xia, H. Li, Appl. Catal., Bl, 268 (2020).
[93] J. Di, P. Song, C. Zhu, C. Chen, J. Xiong, M. Duan, R. Long, W. Zhou, M. Xu, L. Kang, B. Lin, D. Liu, S. Chen, C. Liu, H. Li, Y. Zhao, S. Li, Q. Yan, L. Song, Z. Liu, ACS Mater. Lett. 2 (2020) 1025–1032.
[94] Y. Liu, Z. Hu, J.C. Yu, Chem. Mater. 32 (2020) 1488–1494.
[95] X. Zhong, K.-X. Zhang, D. Wu, X.-Y. Ye, W. Huang, B.-X. Zhou, Chem. Eng. J. 383 (2020).
[96] G. Zhang, L. Zhang, Y. Liu, L. Liu, C.P. Huang, H. Liu, J. Li, ACS Appl. Mater. Interfaces 8 (2016) 26783–26793.
[97] L. Zeng, F. Zhe, Y. Wang, Q. Zhang, X. Zhao, X. Hu, Y. Wu, Y. He, J. Colloid Interface Sci. 539 (2019) 563–574.
[98] Z. Song, X. Dong, J. Fang, C. Xiong, N. Wang, X. Tang, J. Hazard. Mater. 377 (2019) 371–380.
[99] M. Li, Y. Zhang, X. Li, Y. Wang, F. Dong, L. Ye, S. Yu, H. Huang, ACS Sustainable Chem. Eng. 6 (2018) 2395–2406.
[100] F.T. Li, Q. Wang, J. Ran, Y.J. Hao, X.J. Wang, D. Zhao, S.Z. Qiao, Nanoscale 7 (2015) 1116–1126.
[101] F.-T. Li, Y.-L. Li, M.-J. Chai, B. Li, Y.-J. Hao, X.-J. Wang, R.-H. Liu, Catal. Sci. Technol. 6 (2016) 7985–7995.
[102] S. Bai, N. Zhang, C. Gao, Y. Xiong, Nano Energy 53 (2018) 296–336.
[103] Y. Huang, H. Li, W. Fan, F. Zhao, W. Qiu, H. Ji, Y. Tong, ACS Appl. Mater. Interfaces 8 (2016) 27859–27867.
[104] J. Ding, Z. Dai, F. Qin, H. Zhao, S. Zhao, R. Chen, Appl. Catal., B 205 (2017) 281–291.
[105] X. Shi, P. Wang, W. Li, Y. Bai, H. Xie, Y. Zhou, L. Ye, Appl. Catal., B 243 (2019) 322–329.
[106] X. Wu, K. Zhang, G. Zhang, S. Yin, Chem. Eng. J. 325 (2017) 59–70.
[107] X.Y. Kong, W.P.C. Lee, W.-J. Ong, S.-P. Chai, A.R. Mohamed, ChemCatChem 8 (2016) 3074–3081.
[108] N.A. Merino, B.P. Barbero, P. Eloy, L.E. Cadús, Appl. Surf. Sci. 253 (2006) 1489–1493.
[109] D. Cui, L. Wang, K. Xu, L. Ren, L. Wang, Y. Yu, Y. Du, W. Hao, J. Mater. Chem. A 6 (2018) 2193–2199.
[110] M. Cavalleri, K. Hermann, S. Guimond, Y. Romanyshyn, H. Kuhlenbeck, H.J. Freund, Catal. Today 124 (2007) 21–27.
[111] C. Mao, H. Cheng, H. Tian, H. Li, W.-J. Xiao, H. Xu, J. Zhao, L. Zhang, Appl. Catal., B 228 (2018) 87–96.
[112] J. Wu, X. Li, W. Shi, P. Ling, Y. Sun, X. Jiao, S. Gao, L. Liang, J. Xu, W. Yan, C. Wang, Y. Xie, Angew. Chem., Int. Ed. Engl. 57 (2018) 8719–8723.
[113] J. Wang, J. Li, C. Jiang, P. Zhou, P. Zhang, J. Yu, Appl. Catal., B 204 (2017) 147–155.
[114] Y. Zhao, Y. Zhao, R. Shi, B. Wang, G.I.N. Waterhouse, L.Z. Wu, C.H. Tung, T. Zhang, Adv. Mater. 31 (2019).
[115] J. Xiong, J. Di, J. Xia, W. Zhu, H. Li, Adv. Funct. Mater. 28 (2018).
[116] D. Wu, B. Wang, W. Wang, T. An, G. Li, T.W. Ng, H.Y. Yip, C. Xiong, H.K. Lee, P. K. Wong, J. Mater. Chem. A 3 (2015) 15148–15155.
[117] H. Li, J. Shang, Z. Yang, W. Shen, Z. Ai, L. Zhang, Environ. Sci. Technol. 51 (2017) 5685–5694.
[118] L. Wang, D. Lv, F. Dong, X. Wu, N. Cheng, J. Scott, X. Xu, W. Hao, Y. Du, ACS Sustainable Chem. Eng. 7 (2019) 3010–3017.
[119] K. Zhao, L. Zhang, J. Wang, Q. Li, W. He, J.J. Yin, J. Am. Chem. Soc. 135 (2013) 15750–15753.
[120] X.J. Wang, Y. Zhao, F.T. Li, L.J. Dou, Y.P. Li, J. Zhao, Y.J. Hao, Sci. Rep. 6 (2016) 24918.
[121] S. Ge, D. Li, Z. Cui, Y. Zhang, S. Zhang, T. Zhang, G. Jia, W. He, Z. Zheng, Sep. Purif. Technol. 228 (2019).
[122] F. Deng, Q. Zhang, L. Yang, X. Luo, A. Wang, S. Luo, D.D. Dionysiou, Appl. Catal., B 238 (2018) 61–69.
[123] Z. Wei, W. Li, J. Hu, X. Ma, Y. Zhu, J. Hazard. Mater. 402 (2021) 123470.
[124] C. Xiao, X. Qin, J. Zhang, R. An, J. Xu, K. Li, B. Cao, J. Yang, B. Ye, Y. Xie, J. Am. Chem. Soc. 134 (2012) 18460–18466.
[125] S.-Q. Guo, X.-H. Zhu, H.-J. Zhang, B.-C. Gu, W. Chen, L. Liu, P.J.J. Alvarez, Environ. Sci. Technol. 52 (2018) 6872–6880.
[126] W. Li, D. Corradini, M. Body, C. Legein, M. Salanne, J. Ma, K.W. Chapman, P.J. Chupas, A.-L. Rollet, C. Julien, K. Zhagib, M. Duttine, A. Demourgues, H. Groult, D. Dambournet, Chem. Mater. 27 (2015) 5014–5019.
[127] J. Ma, W. Li, B.J. Morgan, J. Świątowska, R. Baddour-Hadjean, M. Body, C. Legein, O.J. Borkiewicz, S. Leclerc, H. Groult, F. Lantelme, C. Laberty-Robert, D. Dambournet, Chem. Mater. 30 (2018) 3078–3089.
[128] W. Zeng, J. Li, L. Feng, H. Pan, X. Zhang, H. Sun, Z. Liu, Adv. Funct. Mater. 29 (2019).
[129] X. Ren, X. Zhang, R. Guo, S. Zhang, L. Wang, X. Pu, Nanotechnology 31 (2020) 495405.
[130] M. Huang, J. Li, W. Su, X. Huang, B. Li, M. Fan, L. Dong, H. He, CrystEngComm 22 (2020) 7684–7692.
[131] V.C. Ferreira, W.R. Wise, O.C. Monteiro, Ceram. Int. 46 (2020) 27508–27516.
[132] J. Li, X.a. Dong, Y. Sun, W. Cen, F. Dong, Appl. Catal., B 226 (2018) 269–277.
[133] F. Rao, G. Zhu, M. Hojamberdiev, W. Zhang, S. Li, J. Gao, F. Zhang, Y. Huang, Y. Huang, J. Phys. Chem. C 123 (2019) 16268–16280.
[134] Y. Huang, H. Hu, S. Wang, M.-S. Balogun, H. Ji, Y. Tong, Appl. Catal., B 218 (2017) 700–708.
[135] Y. Guan, S. Wang, X. Wang, C. Sun, Y. Wang, Z. Ling, RSC Adv. 6 (2016) 2641–2650.
[136] Z. Ma, P. Li, L. Ye, Y. Zhou, F. Su, C. Ding, H. Xie, Y. Bai, P.K. Wong, J. Mater. Chem. A 5 (2017) 24995–25004.
[137] J. Sun, X. Li, Q. Zhao, B. Liu, Appl. Catal., B (2020).
[138] Q. Wu, S. Chai, H. Yang, Z. Gao, R. Zhang, L. Wang, L. Kang, Sep. Purif. Technol. 253 (2020).
[139] X. Li, T. Wang, X. Tao, G. Qiu, C. Li, B. Li, J. Mater. Chem. A 8 (2020) 17657–17669.
[140] H. Yu, D. Ge, Y. Liu, Y. Lu, X. Wang, M. Huo, W. Qin, Sep. Purif. Technol. 251 (2020).
[141] L. Paramanik, K.H. Reddy, K.M. Parida, J. Phys. Chem. C 123 (2019) 21593–21606.
[142] W. Hou, H. Xu, Y. Cai, Z. Zou, D. Li, D. Xia, Appl. Surf. Sci. 530 (2020).
[143] W. Zhao, W. Wang, H. Shi, Appl. Surf. Sci. 528 (2020).
[144] J. Wang, W. Jiang, D. Liu, Z. Wei, Y. Zhu, Appl. Catal., B 176–177 (2015) 306–314.
[145] G. Liu, P. Niu, C. Sun, S.C. Smith, Z. Chen, G.Q. Lu, H.M. Cheng, J. Am. Chem. Soc. 132 (2010) 11642–11648.
[146] X. Ren, M. Gao, Y. Zhang, Z. Zhang, X. Cao, B. Wang, X. Wang, Appl. Catal., B (2020) 274.
[147] J. Ding, Z. Dai, F. Tian, B. Zhou, B. Zhao, H. Zhao, Z. Chen, Y. Liu, R. Chen, J. Mater. Chem. A 5 (2017) 23453–23459.
[148] T. Jia, J. Wu, J. Song, Q. Liu, J. Wang, Y. Qi, P. He, X. Qi, L. Yang, P. Zhao, Chem. Eng. J. 396 (2020).
[149] H. Li, J. Shang, H. Zhu, Z. Yang, Z. Ai, L. Zhang, ACS Catal. 6 (2016) 8276–8285.
[150] Y. Cai, D. Li, J. Sun, M. Chen, Y. Li, Z. Zou, H. Zhang, H. Xu, D. Xia, Appl. Surf. Sci. 439 (2018) 697–704.
[151] L. Li, J. Yan, T. Wang, Z.J. Zhao, J. Zhang, J. Gong, N. Guan, Nat. Commun. 6 (2015) 5881.
[152] B. Sarwan, B. Pare, A.D. Acharya, Appl. Surf. Sci. 301 (2014) 99–106.
[153] H. Li, L. Zhang, Nanoscale 6 (2014) 7805–7810.
[154] S. Zhao, Y. Zhang, Y. Zhou, C. Zhang, X. Sheng, J. Fang, M. Zhang, ACS Sustainable Chem. Eng. 5 (2017) 1416–1424.
[155] L. Ding, R. Wei, H. Chen, J. Hu, J. Li, Appl. Catal., B 172–173 (2015) 91–99.
[156] Y. Yu, C. Cao, H. Liu, P. Li, F. Wei, Y. Jiang, W. Song, J. Mater. Chem. A 2 (2014) 1677–1681.
[157] X. Wang, Q. Ni, D. Zeng, G. Liao, Y. Wen, B. Shan, C. Xie, Appl. Surf. Sci. 396 (2017) 590–598.
[158] H. Wang, W. Zhang, X. Li, J. Li, W. Cen, Q. Li, F. Dong, Appl. Catal., B 225 (2018) 218–227.
[159] W. Wu, Y. Song, L. Bai, Z. Chen, H. Sun, G. Zhen, R. Zhan, Y. Shen, J. Qian, Q. Yuan, Z. Sun, A.C.S. Appl, Nano Mater. 3 (2020) 9363–9374.
[160] Z. Song, X. Dong, N. Wang, L. Zhu, Z. Luo, J. Fang, C. Xiong, Chem. Eng. J. 317 (2017) 925–934.
[161] Y. Yang, Z. Zheng, M. Yang, J. Chen, C. Li, C. Zhang, X. Zhang, J. Hazard. Mater. 399 (2020) 123070.
[162] X. Shi, P. Wang, L. Wang, Y. Bai, H. Xie, Y. Zhou, J.A. Wang, Z. Li, L. Qu, M. Shi, L. Ye, ACS Sustainable Chem. Eng. 6 (2018) 13739–13746.
[163] H. Li, H. Shang, X. Cao, Z. Yang, Z. Ai, L. Zhang, Environ. Sci. Technol. 52 (2018) 8659–8665.
[164] D. Liu, D. Chen, N. Li, Q. Xu, H. Li, J. He, J. Lu, Angew. Chem., Int. Ed. Engl. 59 (2020) 4519–4524.
[165] K.C. Taylor, Catal. Rev. 35 (1993) 457–481.
[166] X.a. Dong, W. Zhang, Y. Sun, J. Li, W. Cen, Z. Cui, H. Huang, F. Dong, J. Catal. 357 (2018) 41–50.
[167] H. Li, H. Shang, Y. Li, X. Cao, Z. Yang, Z. Ai, L. Zhang, Environ. Sci. Technol. 53 (2019) 6964–6971.
[168] Z. Zhao, Y. Cao, F. Dong, F. Wu, B. Li, Q. Zhang, Y. Zhou, Nanoscale 11 (2019) 6360–6367.
[169] L. Zhang, W. Wang, S. Sun, Y. Sun, E. Gao, J. Xu, Appl. Catal., B 132–133 (2013) 315–320.
[170] W.-N. Zhao, Z.-P. Liu, Chem. Sci. 5 (2014) 2256–2264.
[171] J. Xiong, P. Song, J. Di, H. Li, Appl. Catal., B, 256 (2019).

[172] Y. Li, S. Wang, X.S. Wang, Y. He, Q. Wang, Y. Li, M. Li, G. Yang, J. Yi, H. Lin, D. Huang, L. Li, H. Chen, J. Ye, J. Am. Chem. Soc. 142 (2020) 19259–19267.
[173] S. Zhang, Y. Zhao, R. Shi, G.I.N. Waterhouse, T. Zhang, EnergyChem 1 (2019).
[174] C. Mao, H. Li, H. Gu, J. Wang, Y. Zou, G. Qi, J. Xu, F. Deng, W. Shen, J. Li, S. Liu, J. Zhao, L. Zhang, Chem 5 (2019) 2702–2717.
[175] H. Li, J. Shang, J. Shi, K. Zhao, L. Zhang, Nanoscale 8 (2016) 1986–1993.
[176] X. Xue, R. Chen, C. Yan, Y. Hu, W. Zhang, S. Yang, L. Ma, G. Zhu, Z. Jin, Nanoscale 11 (2019) 10439–10445.
[177] H. Wang, B. Zhang, J. Xi, F. Zhao, B. Zeng, Biosens. Bioelectron. 141 (2019) 111443.
[178] Z. Yang, D. Wang, Y. Zhang, Z. Feng, L. Liu, W. Wang, A.C.S. Appl, Mater. Interfaces 12 (2020) 8604–8613.
[179] S. Guan, L. Wang, S.M. Xu, D. Yang, G.I.N. Waterhouse, X. Qu, S. Zhou, Chem. Sci. 10 (2019) 2336–2341.
[180] P. Chen, H. Liu, Y. Sun, J. Li, W. Cui, L.a. Wang, W. Zhang, X. Yuan, Z. Wang, Y. Zhang, F. Dong, Appl. Catal., B (2020) 264.
[181] Y. Fu, D. Sun, Y. Chen, R. Huang, Z. Ding, X. Fu, Z. Li, Angew. Chem., Int. Ed. Engl. 51 (2012) 3364–3367.
[182] S. Liu, J. Xia, J. Yu, ACS Appl. Mater. Interfaces 7 (2015) 8166–8175.
[183] Y. Yang, C. Zhang, C. Lai, G. Zeng, D. Huang, M. Cheng, J. Wang, F. Chen, C. Zhou, W. Xiong, Adv. Coll. Inter. Sci. 254 (2018) 76–93.
[184] A.M. Ganose, M. Cuff, K.T. Butler, A. Walsh, D.O. Scanlon, Chem. Mater. 28 (2016) 1980–1984.
[185] H. Li, F. Qin, Z. Yang, X. Cui, J. Wang, L. Zhang, J. Am. Chem. Soc. 139 (2017) 3513–3521.
[186] Y. Ren, J. Zou, K. Jing, Y. Liu, B. Guo, Y. Song, Y. Yu, L. Wu, J. Catal. 380 (2019) 123–131.